From greenschist to granulite: A mineral equilibria approach to melting and melt loss

Thesis submitted in accordance with the requirements of the University of Adelaide for an Honours Degree in Geology

Kiara Louise Bockmann

November 2015

THE UNIVERSITY of ADELAIDE

FROM GREENSCHIST TO GRANULITE: A MINERAL EQUILIBRIA APPROACH TO MELTING AND MELT LOSS

RUNNING TITLE: MELT LOSS AND MELT REINTEGRATION MODELLING

ABSTRACT

Melt loss during regional high-grade metamorphism has important consequences for interpreting the metamorphic evolution of the lower crust and for understanding processes leading to the chemical differentiation of the crust. However, melt loss typically modifies the protolith; making it difficult to reconstruct the conditions of prograde metamorphism and the extent to which melt loss modified the rock composition. The Reynolds Range in central Australia preserves a rare example where a single melt-prone stratigraphic unit can be traced from greenschist to granulite grade conditions. Using this as a natural laboratory, *P–T* mineral equilibria forward models have been calculated to explore melt loss and melt reintegration where both the protolith and the residuum compositions are preserved. Incremental melt loss modelling from the protolith composition along an isobaric heating path at 5 kbar shows that the residual granulite facies rock composition is consistent with around 18% melt loss from the protolith. Large-scale, one-step melt loss from a closed rock system that had built up 18% melt resulted in a similar residual composition to incremental melt loss. The fertility of the open (incremental) system and the closed system showed the closed system produced 5.4% more melt along a heating path from 700–800 °C. Determination of the concentrations of K–U–Th with increasing metamorphic grade shows that K and U concentrations decreased with increasing metamorphic grade. Conversely, Th concentrations increased, resulting in a slight overall increase in heat production from the protolith to the residuum, despite around 18% volume loss associated with melt extraction. An implication for this is that for melt prone rocks such as metapelites, melt loss during granulite facies metamorphism does not deplete the concentration of heat producing elements in the lower crust as is typically assumed.

KEYWORDS

Metamorphic; Reynolds Range; pseudosection; melt loss; melt reintegration; THERMOCALC; catastrophic melting; heat production

MINERAL ABBREVIATIONS

bi, biotite; mu, muscovite; chl, chlorite; ma, margarite; g, garnet; opx, orthopyroxene; sill, sillimanite; ky, kyanite; and, andalusite; sp, spinel; mt, magnetite; cd, cordierite; liq, silicate melt; ksp, K-feldspar; q, quartz; pl, plagioclase; ep, epidote; ru, rutile; st, staurolite; hem, hematite; ilm, ilmenite.

TABLE OF CONTENTS

LIST OF FIGURES AND TABLES

1. INTRODUCTION

Granulite facies metamorphism within the crust generates melt. A significant proportion of this melt is lost leaving behind a compositional residuum that is depleted in incompatible elements with respect to the original protolith. The process of melt generation and melt loss can greatly affect the compositional evolution of the crust, its rheology and long-term thermal character (e.g. Sighinolfi 1971, Rapp et al. 1991, Brown 1994, Sawyer 1994, Brown and Solar 1998, Sandiford et al. 2002). The important controls on melting and melt loss during regional metamorphism, such as the role of heating rates and deformation are complex and likely to be variable over the timescale of the metamorphic event (England and Thompson 1984, Hanson and Barton 1989). Advances in thermodynamic modelling of mineral assemblages have enabled quantitative forward and inverse modelling of the processes operating in partially molten siliciclastic rocks in increasingly sophisticated chemical systems (Eg. Holland and Powell 2001, White et al. 2001, White et al. 2007, Johnson et al. 2008). These models have been used to investigate the effects of melting and melt loss on crustal rheology, composition and the preservation of geochronometers (Singh and Manglik 2000, Brown 2007, White et al. 2007, Diener et al. 2008). However, the application of these models has been limited to theoretical situations as in almost all real cases there is little information about the composition of the rock prior to melting.

This lack of information about the likely protolith composition also means that it is essentially impossible to determine the prograde *P–T* evolution of a granulite-facies rock, because the composition of the rock in which prograde minerals developed has been irrevocably modified. Previous studies have attempted to model the development of prograde mineral assemblages using an inverse modelling approach in which theoretical compositions of melt are integrated into the rock in order to create a hypothetical ‘protolith’ bulk composition. However, this technique involves many unknowns and relies

heavily on a number of assumptions regarding the prograde metamorphic path and number of melt loss events (White et al. 2004, Korhonen et al. 2013). The determination of a final composition is unconstrained as the prograde compositions no longer exist for comparison.

To test the accuracy of the inverse and forward modelling approaches, a unit preserving both a protolith and residual composition is necessary. This study uses a single metasedimentary unit within the Reynolds Range, Central Australia, which records metamorphism from subsolidus (greenschist) to suprasolidus (granulite) conditions. This provides a natural laboratory to compare calculated compositions from both forward and inverse modelling with the actual rock compositions that span a metamorphic spectrum from greenschist to granulite.

2. GEOLOGICAL BACKGROUND

2.1. Geological setting

The Reynolds Range is a 130 km long, northwest-trending region of outcrop within the Aileron Province in the Arunta region in central Australia (Figure 1; Dirks and Wilson 1990, Clarke and Powell 1991, Hand and Buick 2001, Vry and Baker 2006, Morrissey et al. 2014). It is primarily composed of metasedimentary and granitic rocks that preserve a history of repeated metamorphism and deformation. The oldest rocks in Reynolds Range are the pelitic and psammitic metasedimentary rocks of the Lander Rock Formation which have depositional ages between 1860 and 1840 Ma (Hand and Buick 2001, Claoué-Long et al. 2008, Scrimgeour 2013). Voluminous granitic magmatism between 1810 and 1790 Ma resulted in metamorphism of the Lander Rock Formation at high thermal gradient conditions (Collins and Vernon 1991, Collins and Williams 1995, Rubatto et al. 2001, Worden et al. 2008). The 1810–1790 Ma granitic rocks and the Lander Rock Formation are unconformably overlain by shallow marine successions of the Reynolds Range Group

which was deposited between 1800 and 1780 Ma (Hand and Buick 2001, Claoué-Long et al. 2008, Scrimgeour 2013). The Reynolds Range Group was intruded by voluminous granites at approximately 1780 Ma (Hand and Buick 2001). A second phase of felsic and mafic magmatism occurred at 1790–1770 Ma and was associated with deformation (Howlett et al. In Press). The region experienced pervasive deformation and high thermal gradient metamorphism during the Chewings Event between 1600 and 1530 Ma, which was associated with NE–SW shortening that created the dominant structures in the region (Dirks and Wilson 1990, Vry et al. 1996, Hand and Buick 2001, Rubatto et al. 2001, Anderson et al. 2013, Morrissey et al. 2014).

The final event affecting the Reynolds Range region was the 450–320 Ma Alice Springs Orogeny that resulted in differential exhumation of the terrain, creating a regional metamorphic gradient expressed by differing intensity of 1600–1530 Ma metamorphism (Cartwright et al. 1999, Raimondo et al. 2011). This gradient makes the Reynolds Range region a unique natural laboratory to examine the consequences of progressive metamorphism as it preserves coherent stratigraphy from greenschist to granulite facies metamorphic grade. This study focuses on the pelitic Pine Hill Formation within the Reynolds Range Group (Figure 1). Metapelites have sensitive bulk compositions that can record small changes in *P*–*T* conditions and may produce large volumes of melt during high-grade metamorphism (Bucher and Grapes 2011). Therefore, the Pine Hill Formation provides an unprecedented opportunity to investigate the chemical changes associated with high-grade metamorphism and partial melting, and is the focus of this study.

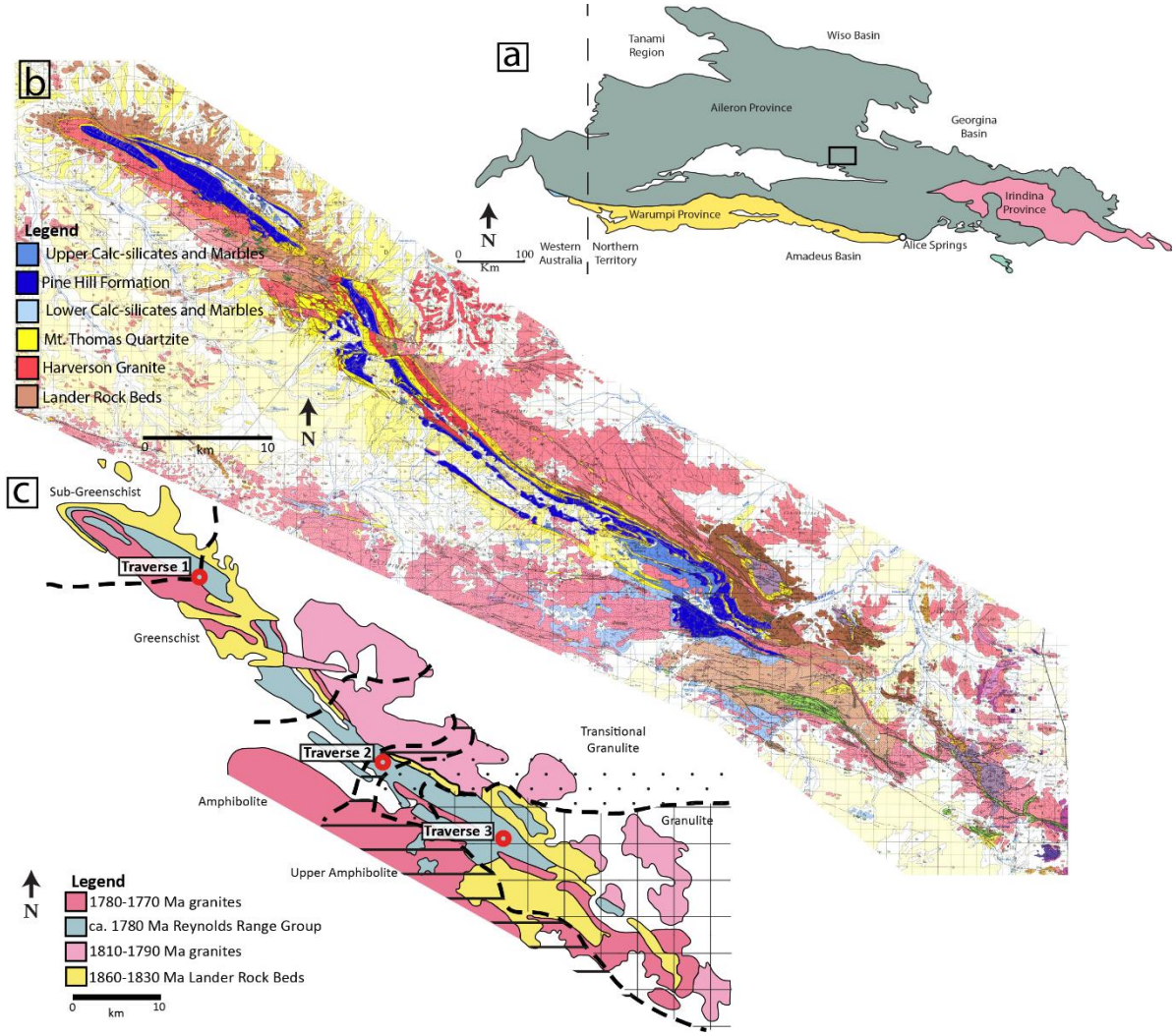

Figure 1. Geology of the Reynolds Range

(a) Simplified map of the Arunta Region showing the location of the Reynolds Range. (b) Detailed geology of the Reynolds Range. The Reynolds Range Group stratigraphy is shown in the inset. Granites ranging in age from 1810–1780 Ma are shown in pink/red (simplified from Stewart et al. 1981). (c) Simplified version of Reynolds Range showing 1600–1530 Ma metamorphic isograds and traverse locations within the Pine Hill Formation.

2.2. Field-based metamorphic geology

The rocks that are the focus of this study are the metapelites of the Pine Hill Formation within the Reynolds Range Group. All rocks are mapped as one continuous, increasingly metamorphosed unit that ranges from greenschist in the northwest to granulite in the southeast (Stewart et al. 1981).

In the north western-most part of the Reynolds Range, the Pine Hill Formation consists of fine-grained biotite–muscovite–chlorite–quartz slate, interlayered with quartzites (Figure

2a). With increasing metamorphic grade moving southeastward the unit contains andalusite and/or cordierite porphyroblasts that are enclosed by the regional foliation, defining the assemblage andalusite–biotite–muscovite–quartz±magnetite±cordierite (Traverse 2). Further southeast in the upper amphibolite-grade rocks andalusite is replaced by sillimanite. The rocks contain minor leucosomes consisting of K-feldspar–plagioclase–quartz±muscovite±tourmaline (Figure 2e, f), interpreted to reflect the onset of partial melting. With a further increase in metamorphic grade both leucosomal segregations and cordierite become more common and the rocks dominantly contain biotite–sillimanite–quartz–magnetite–ilmenite assemblages. At the highest metamorphic grades, cordierite or garnet-bearing leucosomes both parallel and overprint the fabric (Figure 2h, i). The resulting peak granulite facies assemblages are cordierite–biotite–sillimanite–K-feldspar–quartz–ilmenite–(melt) and garnet–biotite–sillimanite–K-feldspar–quartz–ilmenite–(melt).

The Reynolds Range presents an ideal natural laboratory to study the chemical and physical changes that arise from progressive metamorphism and partial melting. The aims of this study are:

(1) To use the Pine Hill Formation within the Reynolds Range Group to examine how progressive partial melting changes the major element chemistry of a metapelitic protolith.

(2) To use the greenschist facies composition of the Pine Hill Formation as a protolith for theoretical forward modelling of melt generation and melt loss within a pelitic bulk composition. This will then be used as a basis to compare theoretically generated bulk compositions arising from melt loss with the actual composition of the Pine Hill Formation residuum after melt was generated and escaped.

(3) To use the composition of the granulite residuum in the Pine Hill Formation as a basis for theoretical modelling of melt reintegration in order to compare the predicted compositions arising from melt reintegration with the actual composition of the sub-solidus Pine Hill Formation.

Aims 1-3 form the main part of this thesis. An additional aim of the project is:

(4) To determine the effect of melt loss within the Pine Hill Formation on the concentration of heat producing elements (K–U–Th). This aim, its methodology and the results are contained in Appendix 1.

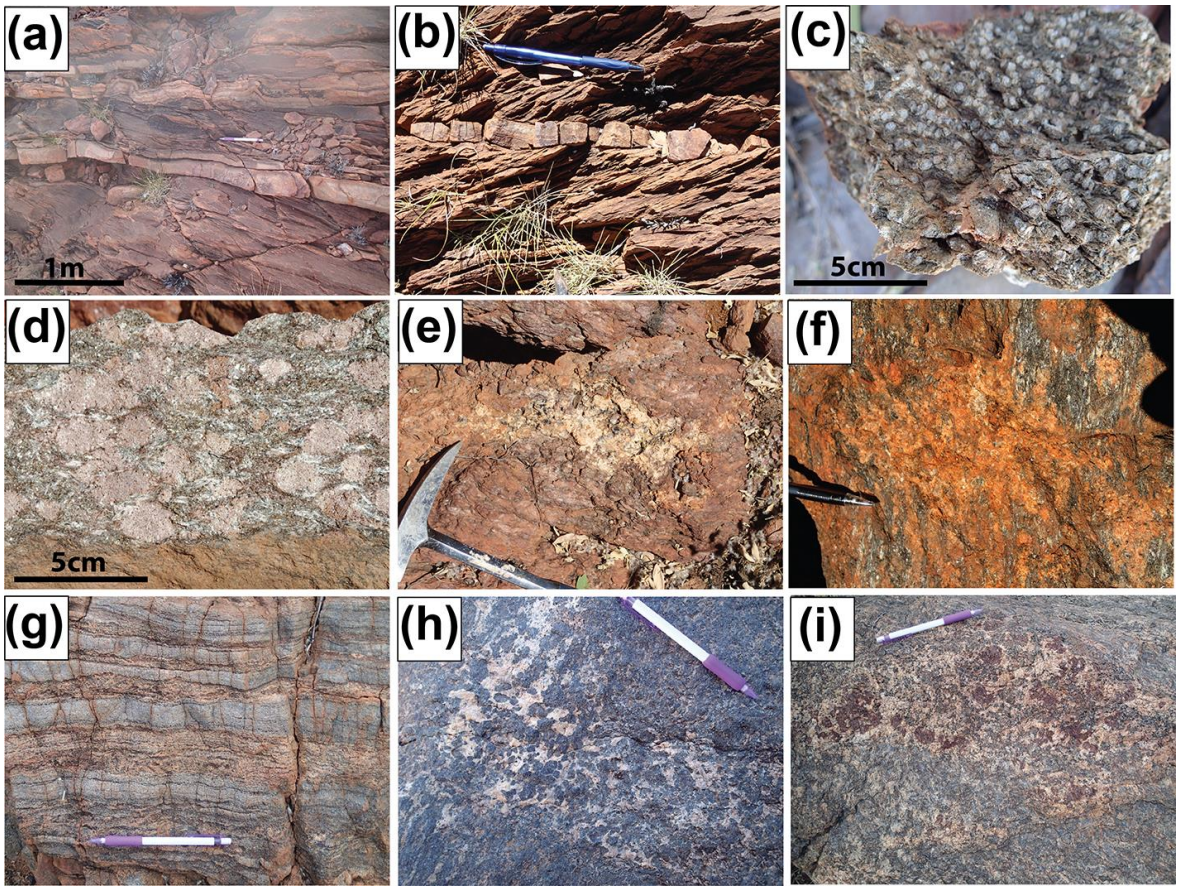

Figure 2. Field photographs of the Pine Hill Formation at different metamorphic grades.

(a) Interbedded pelites and psammites preserving relict sedimentary layering at greenschist facies conditions (Traverse 1). (b) Well developed slaty cleavage transecting a cross-laminated quartzite bed in greenschist facies Pine Hill Formation. (c) Andalusite porphyroblasts enclosed by a biotite-muscovite foliation that is axial surface to the regional SE-trending upright isoclinal folds that deform the Reynolds Range Group (Dirks and Wilson 1990, Hand and Buick 2001). (d) K-feldspar porphyroblasts enclosed by a biotite–sillimanite foliation in upper amphibolite facies Pine Hill Formation (Traverse 2). (e) Leucosome within K-

feldspar–sillimanite–biotite–quartz-bearing upper amphibolite facies Pine Hill Formation interpreted to reflect incipient partial melting. The leucosome contains K-feldspar, quartz, minor plagioclase, muscovite and tourmaline. (f) Leucosome cross-cutting the foliation in the upper amphibolite (Traverse 2.) (g) Relict sedimentary bedding preserved in the granulite facies Pine Hill Formation. Bedding is continuous from cm to m scale in outcrop (Traverse 3). (h) Cordierite porphyroblasts (4–8mm) in a K-feldspar–quartz leucosome in the granulite facies Pine Hill Formation (Traverse 3). (h) Cordierite bearing leucosome in the granulite facies Pine Hill Formation. The matrix around the segregation contains the assemblage biotite–sillimanite–cordierite–K-feldspar–quartz–magnetite (Traverse 3). (h) Garnet bearing leucosome in the granulite facies Pine Hill Formation (Traverse 3).

3. ANALYTICAL METHODS

3.1. Bulk rock and mineral chemistry

The Pine Hill Formation consists of thinly interbedded pelite and psammite layers. Therefore, obtaining representative compositions of the sub solidus Pine Hill Formation, the residual composition in upper amphibolite-grade rocks that had undergone a small amount of partial melting, and the residual composition of the peak metamorphic granulites is problematic. The approach adopted here was to obtain a minimum of 15 samples across traverses perpendicular to the strike of the Pine Hill Formation at greenschist (Traverse 1), upper amphibolite (Traverse 2) and granulite (Traverse 3) grade, choosing samples that appeared to best represent the average character of the formation.

Whole-rock geochemical analyses were obtained for samples from Traverses 1–3 using Wavelength Dispersive X-ray Fluorescence (WD–XRF) spectrometry at the Earth and Environmental Department, Franklin and Marshall College, Lancaster PA, USA. Major elements were analysed by XRF on fused disks prepared using a lithium tetraborate flux. Minor elements were analysed by XRF in briquettes prepared using copolywax. An average of each of the Traverses was taken and used to provide compositions for phase equilibria modelling. The average whole-rock geochemistry for each traverse is given in Table 1 and the complete geochemical analyses are given in Appendix 2.

Chemical analyses of minerals were obtained using a Cameca SX 5 electron microprobe at the University of Adelaide. A beam current of 20 nA for silicates and 100 nA for monazite, and an accelerating voltage of 15 kV was used for all point analyses. Calibration was done on natural and synthetic mineral standards following the standard protocols at Adelaide Microscopy. Representative sample analyses can be found in Appendix 3.

3.2. Mineral equilibria modelling

Pressure-temperature *(P–T)* pseudosections were calculated for the average bulk compositions of samples from Traverse 1 (greenschist) and Traverse 3 (granulite). These compositions were used as the starting point for modelling melt loss and melt reintegration (below). *P–T* pseudosections are forward models that depict the predicted mineral assemblages in a rock of specified bulk composition. *P–T* pseudosections were calculated using the phase equilibrium modelling program THERMOCALC 3.40 (Powell and Holland 1988, Holland and Powell 2011) in the chemical system $MnO–Na_2O–CaO–K_2O–FeO–MgO–Al_2O_3–SiO_2–H_2O–TiO_2–O$ (MnNCKFMASHTO), where 'O' is Fe_2O_3, using the latest internally-consistent thermodynamic dataset ds62' (Holland and Powell 2011) and activity–composition models reparametrised for Mn (Powell et al. 2014, White et al. 2014a, White et al. 2014b).

Calculations in THERMOCALC are based on the user specifying the stable assemblage and calculating the diagram line by line, point by point, where lines (field boundaries) represent the zero abundance of a phase and points represent the zero abundance of two phases. The initial stable assemblage is determined by performing a Gibbs energy minimisation calculation at a set pressure–temperature (*P–T*) condition or by attempting to calculate the stability field of an assemblage that is observed in a sample. The diagram is built up and around that initial assemblage by determining the location in *P–T* space that a

mineral either disappears or a new mineral appears, subject to valid mineral relationships. This involves many trial and error calculations in order to determine which phases appear or disappear as a function of pressure, temperature and/or composition. In addition, the so-called 'starting guesses' (values for variables with which THERMOCALC commences its iterative least-squares calculation for a line or point) require regular updating as the pseudosection is calculated in different parts of *P*–*T*–*X* space (*X* = composition). Therefore, a single diagram commonly comprises >150–200 total line and point calculations, and the user is actively (intellectually), rather than passively, involved in the calculations at every step along the way (typically a model can take several weeks to build).

The largest uncertainties in phase equilibrium modelling relate to the determination of the bulk composition that relates to the peak metamorphic conditions. In particular, the amount of H_2O and Fe_2O_3 is uncertain, as oxidation and hydration during weathering or sample preparation mean that they cannot be adequately measured. For the greenschist calculations, H_2O was considered to be in excess for all sub-solidus calculations. For the purposes of using the greenschist facies composition to model melt loss, the H_2O content was set so that the solidus was just water saturated. For the granulite composition, LOI (Loss on Ignition) was considered to overestimate the amount of H_2O in the bulk composition at the time that the peak mineral assemblage was developed, due to the weathering of many samples and the fact that in granulite-facies terranes it is likely that some of the volatile content of minerals such as biotite and cordierite is not H_2O, but rather CO_2, Cl and F (e.g. Santosh et al. 1993, Rigby and Droop 2011). Instead, H_2O content was determined based on the modal proportion of hydrous minerals (cordierite and biotite) and their H_2O contents. Using point counting, biotite was estimated to compose on average 12% of the whole rock and probe data indicated an average H_2O content of 4 wt% in these samples. Using visual estimates, cordierite was estimated to compose on average 38% of

the whole rock and contain approximately 0.7 wt% H_2O (Buick et al. 1999). This equated to approximately 0.75 wt% H_2O in the bulk composition of the granulite

The oxidation state can have a significant effect on the stability of Fe–Ti oxide minerals such as magnetite, ilmenite and rutile, as well as some silicate minerals (Eg.White et al. 2000, Holland and Powell 2001, Boger et al. 2012, Morrissey et al. 2015). Highly oxidised rocks contain elevated levels of Fe_2O_3, which stabilises minerals such as ilmenite, hematite and magnetite that can incorporate Fe^{3+}. These minerals sequester iron, resulting in the growth of other minerals that are comparatively Mg–Al enriched, such as cordierite. Changes in oxidation state during weathering or sample preparation can cause an overestimation of the amount of Fe_2O_3 in the bulk composition when it is determined by titration (Johnson and White 2011, Lo Pò and Braga 2014). Therefore, the amount of Fe_2O_3 was determined based on the mineral assemblage and an assessment of the Fe^{3+} content of the minerals. For the average greenschist composition from Traverse 1, 5% of the total Fe value was estimated to be Fe_2O_3, based on the absence of magnetite in these samples. For the average granulite composition from Traverse 3, 20% of the total Fe value was estimated to be Fe_2O_3, based on the presence of both magnetite and ilmenite in these samples and their approximate proportions. The effect of oxidation state on the mineral relationships was investigated using a $T–M_o$ section (where M_O refers to the amount of a particular variable that is modelled against temperature at a set pressure; in this case O was modelled at 5 kbars) calculated for the third melt loss composition (approximately equivalent to the residual granulite composition).

3.2.1 MELT LOSS AND MELT REINTEGRATION MODELLING

Intact relict cm-scale sedimentary layering in the granulites shown in Figure 2g suggests that melt loss from the rock was likely to have been relatively efficient, without the

accumulation of large amounts of melt that would have resulted in catastrophic melt loss that would destroy the small scale sedimentary-derived layering (e.g. Johnson et al. 2011). The melt connectivity transition (MCT) threshold (approximately 7%); Rosenberg and Handy (2005) was used as a maximum for melt loss and melt reintegration calculations, where melt is extracted when it reaches 7% of the rock's total volume. However, in the presence of syn-anatectic deformation, melt extraction is likely to occur at a lower threshold (White et al. 2001, White et al. 2007, Brown 2010, Korhonen et al. 2013). The MCT is defined as the amount of melt required to create a connected grain boundary network in a rock that results in the rapid decrease of the rock's strength (Rosenberg and Handy 2005).

For the purpose of melt loss and melt reintegration modelling, an isobaric heating path at 5 kbar was assumed. Morrissey et al. (2014) suggest that peak pressures in the south-eastern Reynolds Range, approximately 20 km east of Traverse 3 (Figure 1), reached a maximum of 6.5 kbar. In the central Reynolds Range andalusite has been pseudomorphed by sillimanite, suggesting prograde pressures of approximately 3.8 kbar (e.g. Figure 4). If a constant *P*–*T* gradient is assumed between these two locations, then the pressure conditions at the first point of melting would have been approximately 5 kbar.

Melt loss modelling was undertaken using the methodology of Yakymchuk and Brown (2014b), whereby melt is removed in a stepwise fashion from the initial bulk composition when it reaches a modal proportion of 7 mol%. At this point, 6 mol% melt is removed from the system leaving 1 mol% melt in the composition, interpreted to be the amount of melt retained on grain boundaries (Holness and Sawyer 2008). The composition is then normalised and a new pseudosection is calculated using the melt depleted composition. This process is repeated until a desired end point is reached. In this study the end point was

the removal of 18% melt, with attainment of a granulite facies mineral assemblage that approximates that observed in Traverse 3. However, in principal the modelling could be continued until a completely melt infertile composition for attainable crustal *P–T* conditions is reached.

Melt reintegration modelling was undertaken using the methodology of Korhonen et al. (2013) to investigate the differences and similarities between forward and inverse modelling along the same compositional unit. This method adds 6 mol% melt to the system when the modal proportion of melt in the initial composition reaches 1 mol%. This is the reverse process of the melt loss modelling of Yakymchuk and Brown (2014b). The resulting composition is then normalised and can be used to calculate further *P–T* models until the composition produces a wet solidus. The composition of the reintegrated melt corresponds to the composition of the 1% melt fraction present when melt is reintegrated.

3.3. KUTh concentration

The concentrations of the heat producing elements K, U and Th (KUTh) were measured using three portable Gamma Ray Spectrometer (GRS) devices. The calibrated GRS devices were placed on well-exposed outcrops and allowed to assay for 180 seconds, to gain an accurate reading of the quantities of heat producing elements (HPEs) in close proximity to the devices. Further details on KUTh concentration data collection can be found in Appendix 1.

4. RESULTS

4.1. Metamorphic geology

4.1.1. METAMORPHIC PETROGRAPHY

Samples were taken across the strike of three traverses through the Pine Hill Formation (Figure 1). Peak and retrograde mineral assemblages have been interpreted on the basis of mineralogy and microstructural context.

Traverse 1 (greenschist facies)

Samples RR2014-1A–5D

These samples contain biotite, muscovite, chlorite, quartz, rutile, ilmenite and minor epidote. All traverse 1 samples are homogeneous and fine grained (<0.5 mm) and contain a pervasive foliation defined by muscovite, biotite and minor chlorite (Figure 3a). The relative amounts of biotite, muscovite and chlorite are variable but samples are typically dominated by muscovite. The remainder of each of the samples is comprised of quartz. The majority of samples contain ilmenite, though some samples contain rutile with no ilmenite. The peak assemblage is interpreted to be biotite–muscovite–chlorite–quartz±rutile±ilmenite.

Traverse 2 (upper amphibolite facies)

Samples RR2015-1-1 – 26

These samples contain biotite, muscovite, K-feldspar, quartz, sillimanite, tourmaline and ilmenite. Sillimanite forms large fibrous masses that appear to have pseudomorphed another mineral; likely to have been andalusite. Interlayered sillimanite and biotite define the foliation (Figure 3e). Coarse crystals of muscovite overprint the foliation in some samples and are likely to be a retrograde phase after K-feldspar and sillimanite. K-feldspar

is partially altered in many of these samples to sericite and hematite and forms large crystals (8–15 mm) with quartz and biotite inclusions. K-feldspar also occurs as smaller crystals intergrown with quartz (2–6 mm) that form between biotite grains. Rare tourmaline grains (3–8 mm) occur as anhedral crystals with K-feldspar and biotite. Many of the minerals in these samples have been overprinted by low-*T* sericitic alteration (Figure 3d), which may account for the elevated average K_2O content and LOI compared to the greenschist and granulite grade parts of the Pine Hill Formation (Table 1). The peak assemblage is interpreted to be biotite–K-feldspar–quartz–sillimanite–ilmenite.

Traverse 3 (granulite facies)

Samples RR2014-6A– 12A

These samples contain biotite, cordierite, magnetite, sillimanite, garnet and K-feldspar. They contain a weak gneissic fabric primarily defined by biotite and sillimanite. Biotite is almost always in contact with or included within cordierite and K-feldspar. Sillimanite commonly occurs as patches of unoriented needles, included within cordierite and K-feldspar (Figure 3g), but also as a second generation that occurs as much larger grains (>10 mm long) that define the fabric. Cordierite is abundant and is in contact with all other minerals. Garnet is only present in some samples. Garnet is generally wrapped by the sillimanite–biotite fabric and often contains inclusions of quartz (Figure 3f). K-feldspar and quartz occur as small grains (1–2 mm) and may be included within magnetite or cordierite. Magnetite grains (2–5 mm) commonly occur on the edge of biotite and sillimanite grains. Rare, small grains (<1 mm) of chlorite may occur in contact with biotite or sillimanite and are interpreted to be retrograde. The peak assemblage is interpreted to be biotite–sillimanite–cordierite–garnet–K-feldspar–quartz–magnetite–ilmenite.

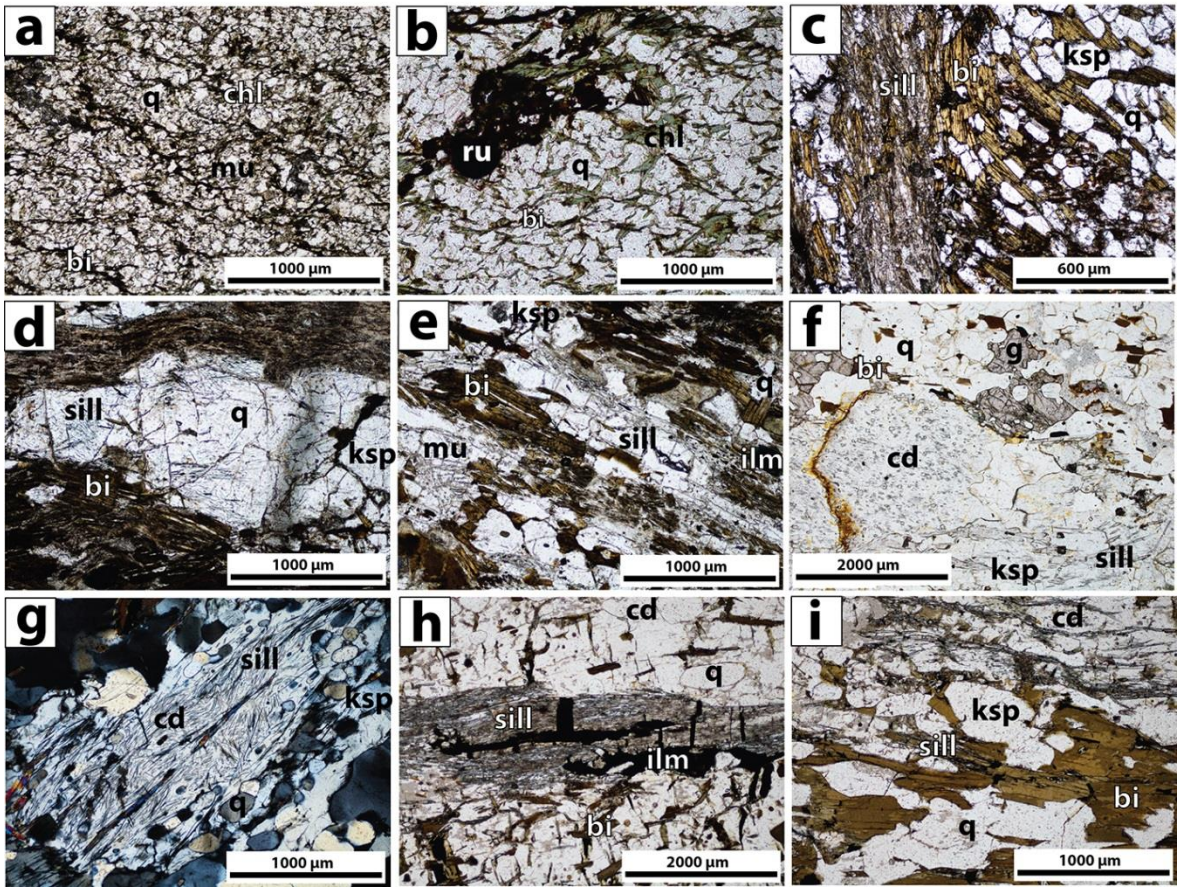

Figure 3. Photomicrographs of mineral relationships in the Pine Hill Formation.

(a) Greenschist facies: Fine grains of quartz, chlorite, muscovite and biotite. (b) Greenschist facies: Rutile surrounded by quartz and biotite and minor chlorite. (c) Upper amphibolite facies: Interlayered sillimanite and biotite form the primary foliation. Grains of K-feldspar and quartz form layers between the biotite. (d) Upper amphibolite facies: Fine needles of sillimanite included within quartz and K-feldspar, wrapped in the biotite foliation. (e) Upper amphibolite facies: Large masses of sillimanite needles interlayered with biotite to form the primary fabric. K-feldspar and quartz grains are wrapped in the fabric as well as uncommon grains of muscovite. (f) Granulite Facies: Garnet surrounded by quartz and biotite. Cordierite has many K-feldspar and quartz inclusions, with sillimanite inclusions primarily located in K-feldspar. (g) Granulite Facies: Cordierite contains abundant inclusions of sillimanite and less commonly ilmenite and biotite. (h) Granulite Facies: Ilmenite associated with foliation defining sillimanite, surrounded by quartz and cordierite. Biotite is randomly orientated and generally included within cordierite. (i) Granulite Facies: Large biotite grains surrounded by sillimanite, K-feldspar and cordierite. Aggregates of fine-grained sillimanite define the foliation and are interlayered with cordierite.

4.1.2. GEOCHEMISTRY AND MINERAL CHEMISTRY

Whole-rock geochemical data are provided in Appendix 2. Full analyses for electron-microprobe mineral compositions used for phase equilibria modelling are given in Appendix 3.

Table 1. Average bulk rock compositions from each traverse in wt%.

	Greenschist	Upper amphibolite	Granulite
Major elements (wt%)			
SiO_2	69.28	64.82	66.43
TiO_2	0.49	0.68	0.76
Al2O_3	14.35	19.55	18.45
Fe_2O_3T	6.39	6.97	5.68
MnO	0.04	0.06	0.03
MgO	1.78	1.93	3.94
CaO	0.06	0.10	0.09
Na_2O	0.09	0.27	0.09
K_2O	4.54	5.30	3.55
P_2O_5	0.09	0.07	0.06
LOI	3.00	4.14	1.40
Total	**99.83**	**99.74**	**99.01**
Trace elements (ppm)			
Rb	279	379	185
Sr	24	38	22
Y	24	25	15
Zr	193	147	267
V	66	91	98
Ni	33	61	49
Cr	61	118	84
Nb	13	16	16
Ga	22	28	30
Cu	33	22	14
Zn	57	48	22
Co	17	24	19
Ba	663	395	612
La	40	34	28
Ce	87	70	61
U	1	1	1
Th	29	31	31
Sc	10	13	11
Pb	4	3	9

LOI, Loss on Ignition; Fe_2O_3T, total FeO and Fe_2O_3

4.2. PRESSURE-TEMPERATURE PSEUDOSECTIONS

The 1600–1530 Ma Chewings Event resulted in progressive metamorphism of the Pine Hill Formation along a high thermal gradient, culminating in an anatectic granulite facies assemblage in the southeastern Reynolds Range (Hand and Buick 2001, Morrissey et al. 2014). The preservation of granulite facies mineral assemblages (Figure 3) imply that melt

was generated, but also lost from the granulite (e.g. White and Powell 2002).

As a framework for the analysis of the Pine Hill Formation's response to metamorphism, Figures 4 and 10 show the *P–T* forward models for the greenschist bulk composition in a closed system (i.e. melt does not escape), and for the residual bulk composition of the granulite. These compositions were used as starting points for melt loss and melt reintegration modelling, as well as comparisons for final modelled compositions where melt had been extracted or reintegrated.

4.2.1. MELT LOSS

The effects of progressive melt loss along an inferred prograde heating path at 5 kbar are shown in Figures 5–7. The composition of melt within a given rock is dependent on the *P–T* conditions, and the removal of melt modifies the composition and fertility of the source rock. Therefore, the effects of progressive melt loss along an inferred isobaric heating path at 5 kbar were modelled using a series of *P–T* pseudosections. The composition of melt was calculated at 5 kbar when the amount of melt in the rock reached 7 mol%. All but 1 mol% of this melt was then extracted and the residual composition used to calculate a new melt-bearing *P–T* pseudosection. This process was repeated three times, with a total of 18 % melt removed from the original greenschist bulk composition. After the third melt loss extraction (Figure 7) the composition no longer produced the assemblage observed in the majority of the granulite facies samples, suggesting that melt loss in the Pine Hill Formation did not exceed approximately 20%.

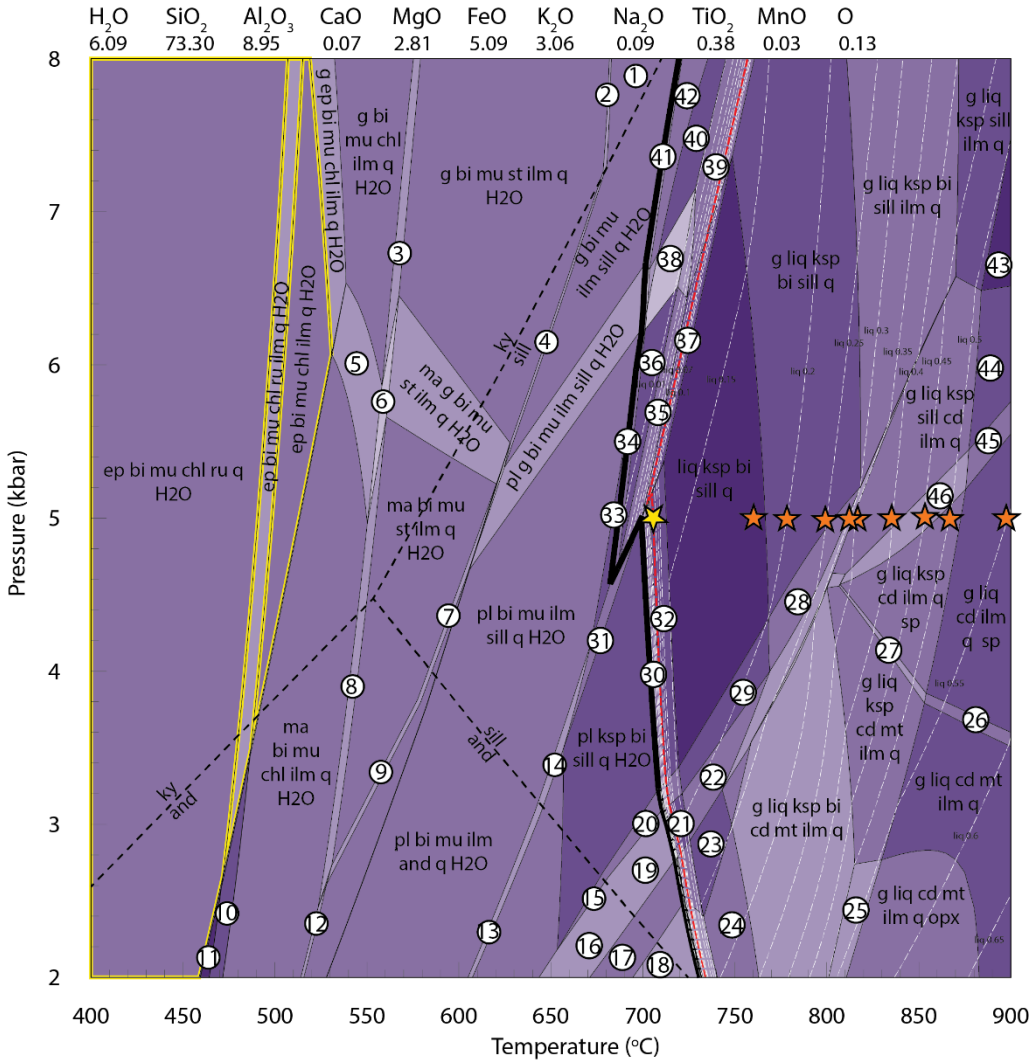

*Small fields not labelled

1. g bi mu ilm ky q H2O
2. g bi mu ilm ky st q H2O
3. g bi mu st ilm q chl H2O
4. g bi mu ilm sill q st H2O
5. g bi mu chl ilm q ma H2O
6. g bi mu chl ilm q ma st H2O
7. ma bi mu st ilm q sill H2O
8. ma ep bi mu chl ilm q st H2O
9. ma bi mu st ilm q and H2O
10. ma bi mu chl ilm q ru H2O
11. bi mu chl ru q ma H2O
12. ma bi mu chl ilm q and H2O
13. pl bi mu ilm and q ksp H2O
14. pl ksp bi ilm sill q mu H2O
15. pl ksp bi and q cd H2O
16. pl ksp bi cd ilm q and H2O
17. pl ksp bi cd ilm q H2O
18. pl ksp bi cd ilm q H2O mt
19. pl ksp bi cd ilm q H2O sill
20. pl ksp bi cd q H2O sill
21. ksp bi cd ilm q H2O liq sill
22. liq ksp bi cd ilm q sill
23. liq ksp bi cd ilm q
24. liq ksp bi cd mt ilm q
25. g liq cd mt ilm q opx ksp
26. g liq cd mt ilm q sp
27. g liq ksp cd mt ilm q sp
28. g liq ksp bi sill q cd
29. liq ksp bi sill q cd
30. pl ksp bi sill q liq
31. pl ksp bi sill q mu H2O
32. liq ksp bi cd sill q H2O
33. pl bi sill q mu
34. pl bi sill q mu liq
35. pl bi sill q mu liq H2O ksp
36. pl bi sill q mu liq H2O
37. liq ksp bi sill q mu pl
38. g bi mu sill q liq H2O pl
39. g bi mu sill q liq H2O ksp
40. g bi mu sill q liq H2O
41. g bi mu ilm sill q liq
42. g bi mu ilm sill q liq H2O
43. g liq ilm sill q
44. g liq ilm sill q cd
45. g liq ilm sill q cd sp
46. g liq ilm sill q cd sp ksp

Figure 4. Calculated *P–T* pseudosection for greenschist protolith.

The bulk composition (in mol %) was calculated as an average from samples RR2014-1A – RR2014-5d and is given above the pseudosection. The fields 10 and 11, outlined in yellow, indicate the interpreted peak assemblage in the greenschist rocks. The bold black line represents the solidus. The modal proportion of liquid above the solidus is represented by the white dashed lines. The red dashed line represents the 7 percent liquid threshold, where melt was extracted for subsequent calculations. The yellow star represents the *P–T* conditions that melt was extracted at 5 kbar and 705.66 °C. Each of the orange stars represent the *P–T* conditions that melt was extracted for catastrophic melt loss event (see text below), shown in Figure 9 and Appendix 5.

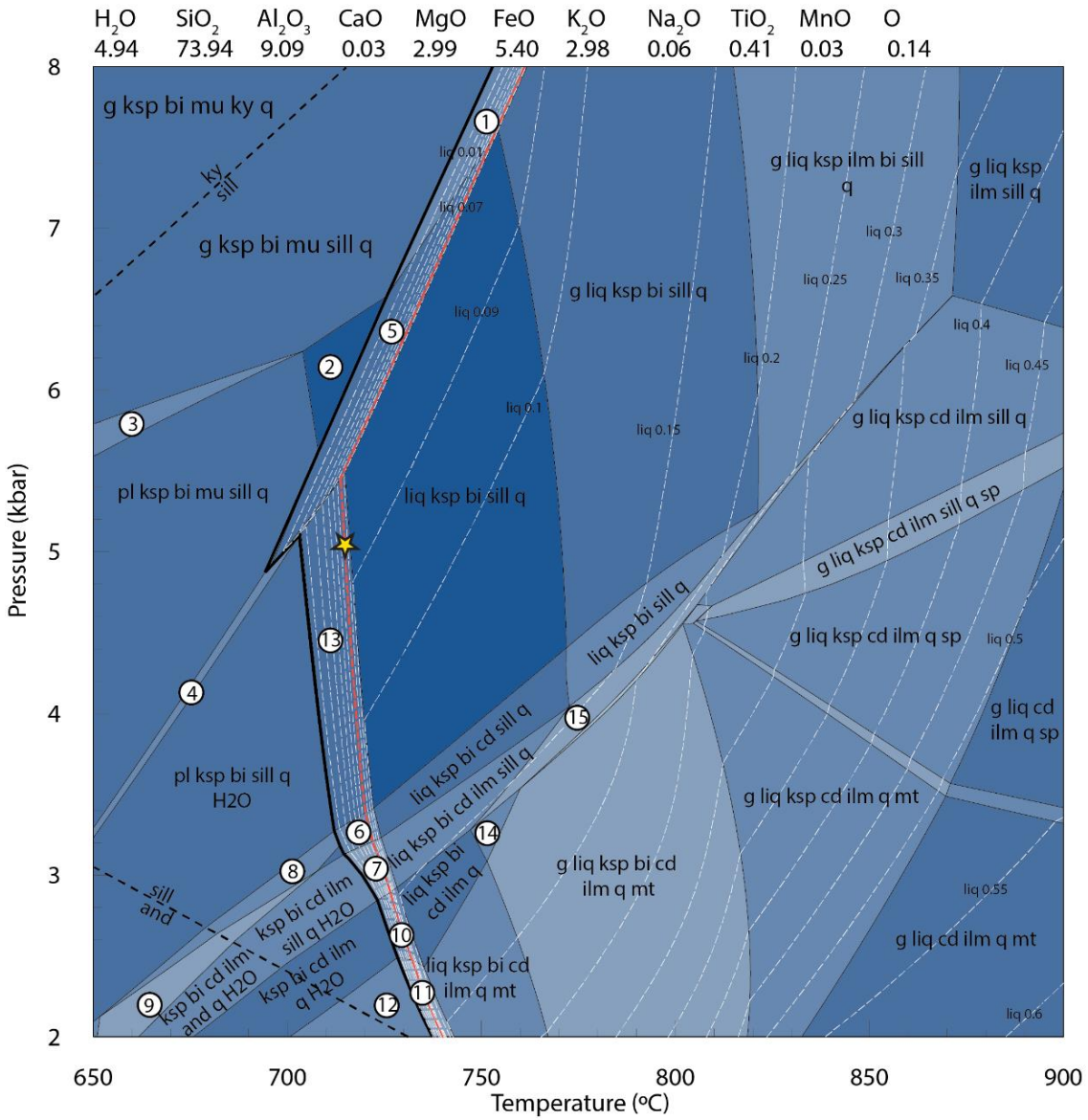

*Small fields not labelled

1. g liq ksp bi mu sill q
2. ksp bi mu sill q
3. g pl ksp bi mu sill q
4. pl ksp bi mu sill q H2O
5. liq ksp bi mu sill q
6. liq ksp bi cd sill q H2O
7. liq ksp bi cd ilm sill q H2O
8. pl ksp bi cd sill q H2O
9. pl ksp bi cd ilm sill q H2O
10. liq ksp bi cd ilm q H2O
11. liq ksp bi cd ilm q mt H2O
12. ksp bi cd ilm q mt H2O
13. liq ksp bi sill q H2O
14. g liq ksp bi cd ilm q
15. liq ksp bi sill g q

Figure 5. Calculated *P–T* pseudosection after first stage melt loss (6 % removed).

The bulk composition (in mol%) was calculated after the extraction of 6 percent melt from the greenschist protolith and is given above the pseudosection. The bold black line represents the solidus. The modal proportion of liquid above the solidus is represented by white dashed lines. The red dashed line represents the 7 mol% melt threshold, where melt was extracted for subsequent calculations. The yellow star represents the *P–T* conditions of the second melt loss event at 5 kbar and 714.94 °C.

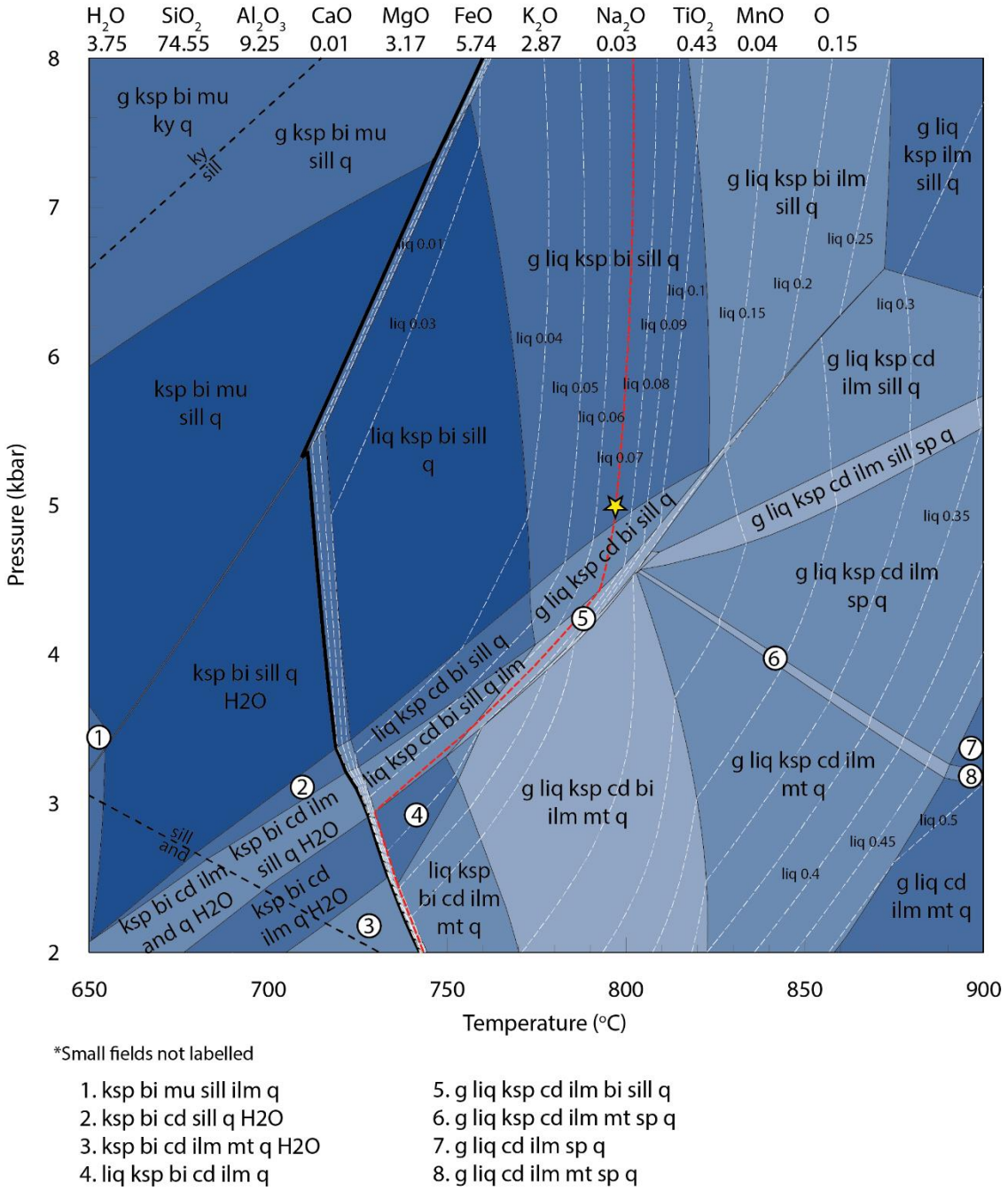

*Small fields not labelled

1. ksp bi mu sill ilm q
2. ksp bi cd sill q H2O
3. ksp bi cd ilm mt q H2O
4. liq ksp bi cd ilm q
5. g liq ksp cd ilm bi sill q
6. g liq ksp cd ilm mt sp q
7. g liq cd ilm sp q
8. g liq cd ilm mt sp q

Figure 6. Calculated *P–T* pseudosection after second stage melt loss (12 % removed).

The bulk composition (in mol%) after extraction of 12 mol% melt is given above the pseudosection. The bold black line represents the solidus. The modal proportion of liquid above the solidus is represented by white dashed lines. The red dashed line represents the 7 percent liquid threshold, where melt was extracted for subsequent calculations. The yellow star represents the *P–T* conditions that melt was extracted at 5 kbar and 797.17 °C.

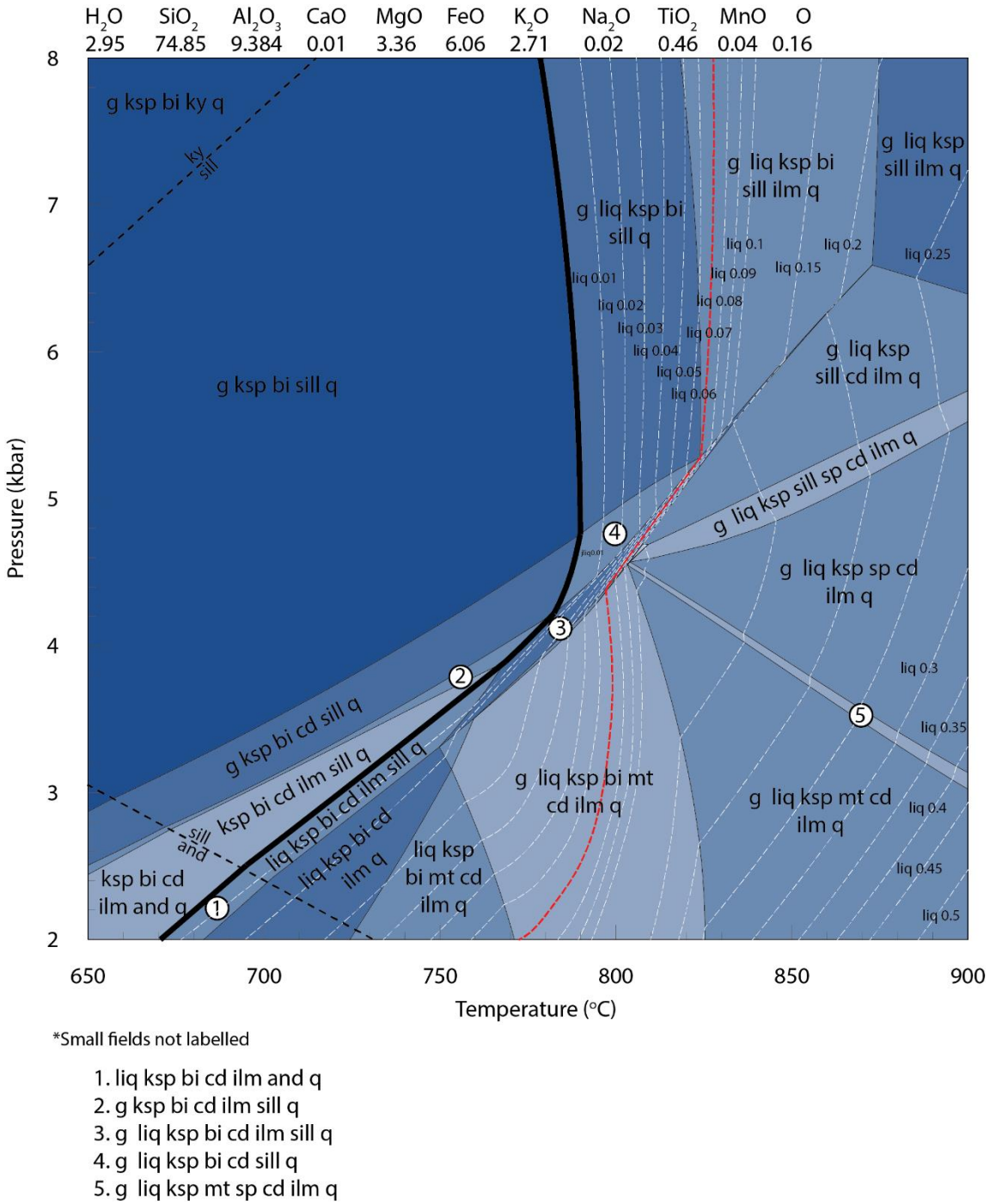

*Small fields not labelled

1. liq ksp bi cd ilm and q
2. g ksp bi cd ilm sill q
3. g liq ksp bi cd ilm sill q
4. g liq ksp bi cd sill q
5. g liq ksp mt sp cd ilm q

Figure 7. Calculated *P–T* pseudosection after third stage melt loss (18 % removed).

The bulk composition (in mol%) after extraction of 18 mol% melt is given above the pseudosection. The bold black line represents the solidus. The modal proportion of liquid above the solidus is represented by white dashed lines. The red dashed line represents the 7 percent liquid threshold, where melt would be extracted for further calculations

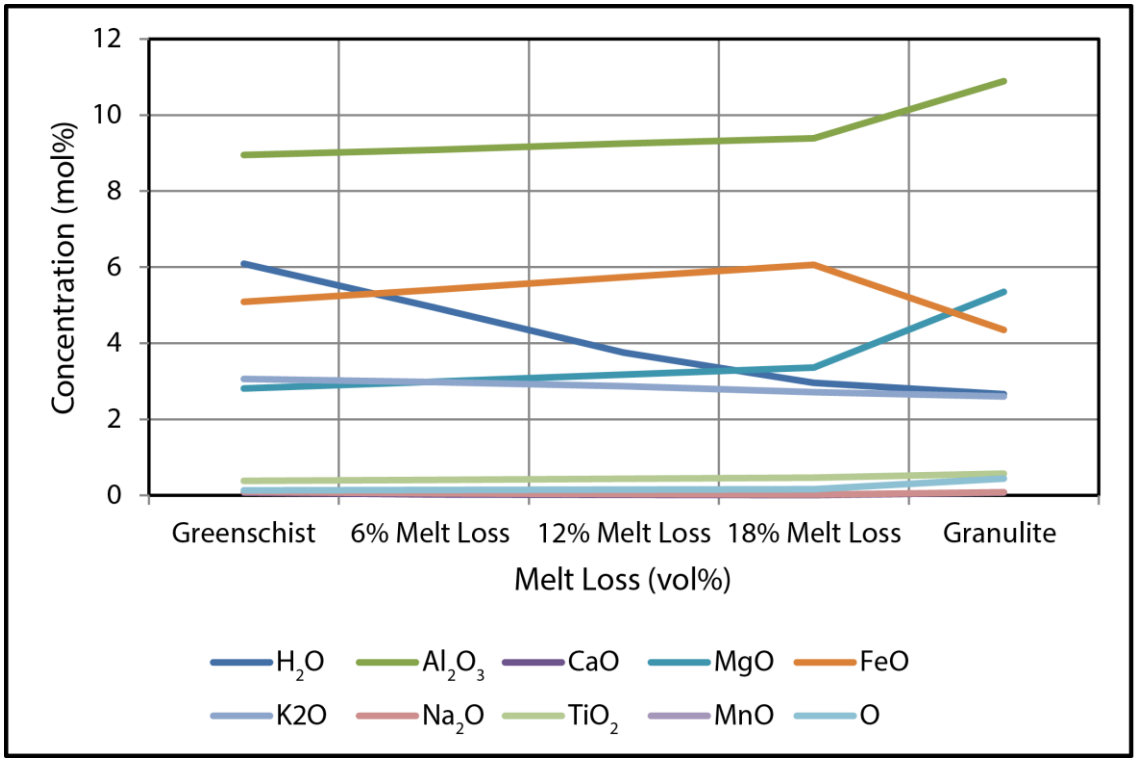

Figure 8. Changing element concentrations with progressive melt loss.

The average greenschist bulk composition is given as a starting point and the average granulite bulk composition as the end point.

The composition of the melt that is extracted from a rock is largely dependent on the original composition of the rock itself. The melt compositions extracted from each of the models above (Figures 4–6) are shown in Table 2. All of the melts primarily consist of H_2O, SiO_2, Al_2O_3 and K_2O, with minor amounts of CaO, MgO, MnO, FeO and Na_2O. The melts become slightly more silicious, more potassic and less hydrous as the rock composition becomes more residual, whereas aluminium content in the melt remains approximately the same.

In a perfect experiment in which the Pine Hill Formation had exactly the same protolith composition along its entire length, and the thermodynamic data and activity-composition for minerals and melt are entirely correct (e.g. Powell and Holland 1988, Johnson et al. 2003, Zuluaga et al. 2005, White et al. 2007), the concentration of each element should track away from the original greenschist bulk composition and toward the observed

composition of the granulite. Partial melting and melt loss results in the concentration or depletion of elements in the residuum. Figure 8 shows the computed compositional changes in the modelled residuum compared to the actual composition of the residual granulite. The melt loss modelling shown in Figures 5–7 results in a number of elements tracking from the greenschist towards the granulite composition, including H2O, SiO2, K2O, TiO2 and MnO. However, some elements such as Al2O3, CaO, MgO, FeO and Na2O did not track towards the granulite composition, and the removal of 18 % melt increased the difference in concentration. A summary of the compositions after successive melt loss events is given Appendix 4. Progressive melt loss also resulted in elevation of the solidus to higher temperatures.

Table 2. Compositions of the melt that was extracted from each progressive melt loss model (Figures 4-6) in wt%.

	Greenschist Melt (after 6 % melt extraction)	**Melt loss 1 melt (after 12 % melt extraction)**	**Melt loss 2 melt (after 18 % melt extraction)**
H_2O	8.05	7.87	5.10
SiO_2	70.06	70.97	72.35
Al_2O_3	12.65	12.09	12.55
CaO	0.71	0.30	0.06
MgO	0.02	0.02	0.13
MnO	0.11	0.00	0.00
FeO	0.00	0.13	0.73
K_2O	7.63	8.09	8.83
Na_2O	0.77	0.52	0.26
TiO_2	0.00	0.00	0.00
Fe_2O_3	0.00	0.00	0.00
ZrO_2	0.00	0.00	0.00

4.2.1.1. Catastrophic melt loss

The previous section investigated the compositional consequences of progressive melt loss. However, as the likely threshold for melt loss is difficult to constrain, the consequences of catastrophic melt loss on the residuum composition were also investigated. Catastrophic melt loss is defined here as melt loss from a system containing melt volumes well above the percolation threshold (7 mol%). Catastrophic melt loss events were calculated using the

initial greenschist composition and a closed system, and involved removing all but 1 mol% of the melt at once for a range of different melt volumes between 0 and 55 mol% of the rock's total volume (Figure 9 and Appendix 5). The removal of 18 % melt incrementally or catastrophically resulted in little to no difference in the final composition.

As with the incremental melt loss, catastrophic melt loss resulted in an overall increase in the concentration of Al_2O_3, MgO, FeO, TiO_2, MnO and O and a decrease in the concentration of H_2O, SiO_2, CaO, K_2O, and Na_2O.

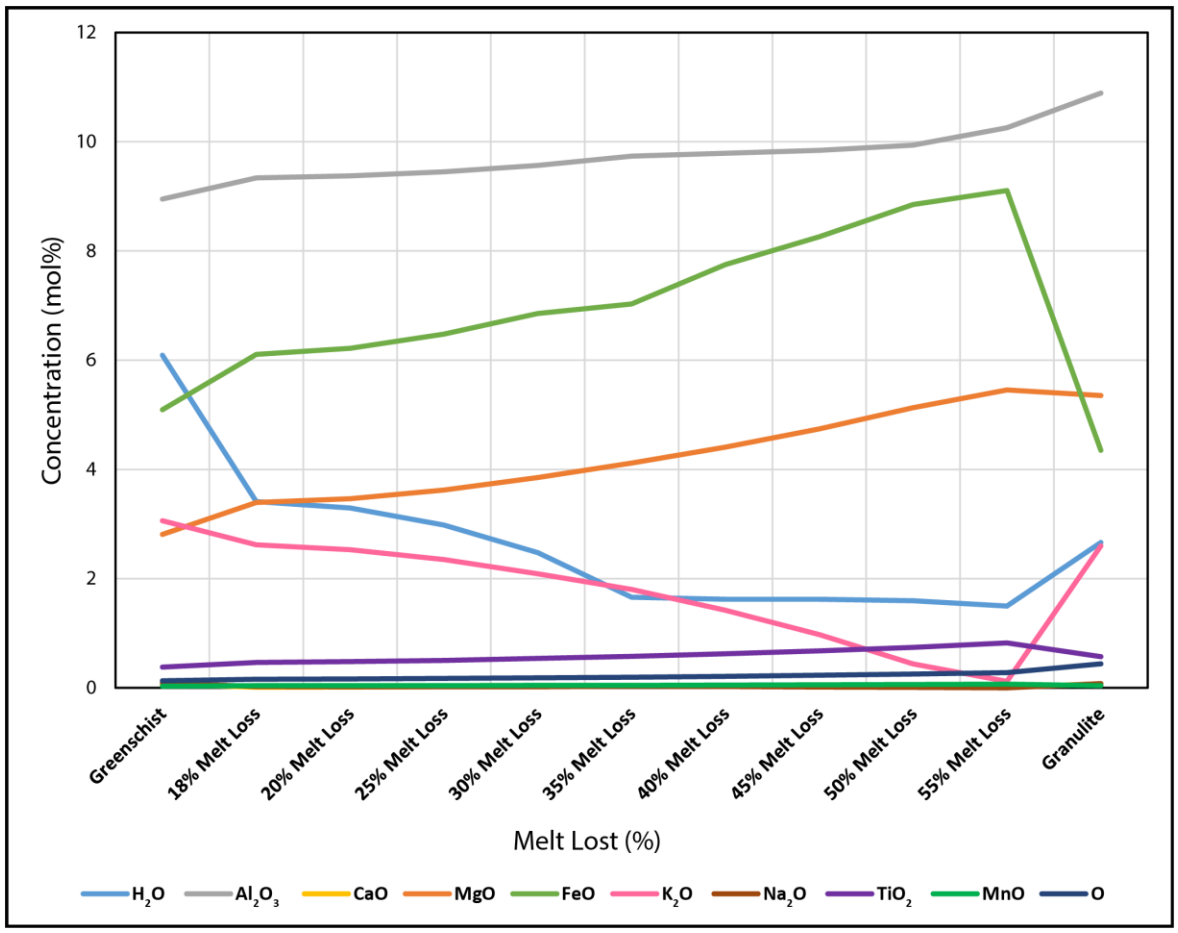

Figure 9. Elemental concentrations in residuum after varying amounts of catastrophic melt loss.

The average greenschist bulk composition is given as a starting point and the average granulite bulk composition as the end point.

4.2.2. MELT REINTIGRATION

Essentially all *P–T* studies on granulites are based on residual rock compositions that have been irrevocably altered by melt loss, and are therefore no longer relevant to the

composition in which much of the preserved mineralogy developed. This precludes effective modelling of the prograde *P–T* history. To reconstruct a plausible bulk composition, pre-melt loss, a realistic melt composition can be reintegrated back into the rock (e.g. Korhonen et al. 2013).

P–T pseudosections were calculated for three successive melt reintegration events along an isobaric cooling path at 5 kbar, beginning after the first addition of melt to the residual granulite composition (Figures 10–13). When the modal proportion of melt in the model reached 1 mol% the composition of the melt was calculated and an extra 6 mol% added, to mimic the 7 % MCT (Rosenberg and Handy 2005). The new composition was then used to calculate further *P–T* pseudosections and the process repeated. Melt was reintegrated three times, with a total of 18 mol% melt added to the original granulite. This reintegration procedure resulted in the formation of a H_2O saturated solidus, which is the likely case that would have existed when the rocks crossed the solidus on the prograde path. Figure 14 shows the compositional consequences of the reintegration of melt back into the average residual bulk composition.

Melt reintegration modelling resulted in a number of elements tracking from the granulite composition towards the greenschist composition, including H_2O, Al_2O_3, MgO, K_2O, TiO_2 and MnO. Other elements, including SiO_2, CaO, FeO and Na_2O, did not track towards the greenschist composition and the reintegration of melt increased the difference between the greenschist and granulite compositions. The interpreted peak mineral assemblage of the original greenschist facies samples was not reached after 18 mol% of the melt had been reintegrated. A summary of calculated melt reintegration bulk compositions is given in Appendix 7.

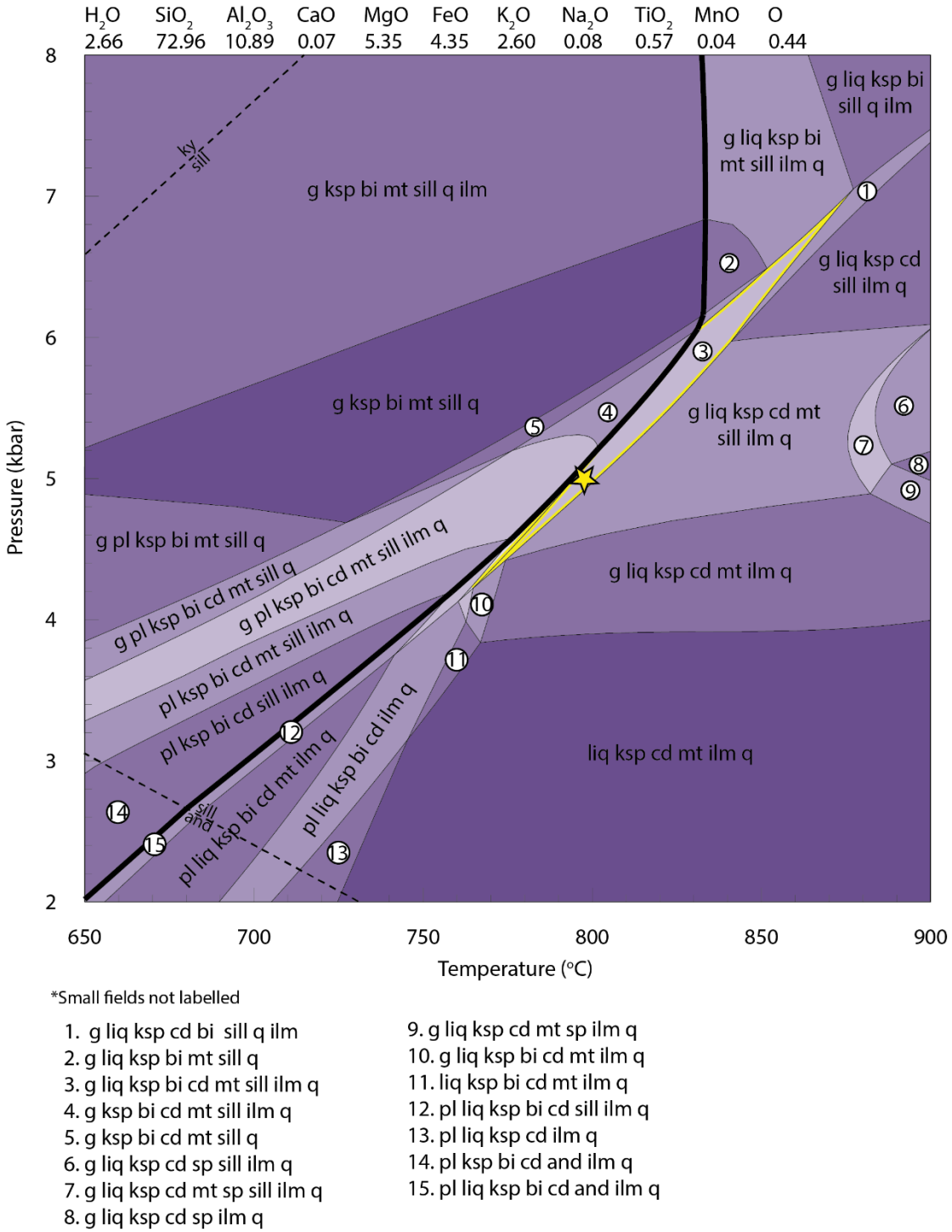

Figure 10. Calculated *P–T* pseudosection for the average granulite bulk composition.

The bulk composition (in mol%) was calculated as an average from samples RR2014-6D–RR2014-12a and is given above the pseudosection. The bold black line represents the solidus. The field outlined in yellow is the interpreted peak assemblage of the sample. The yellow star represents the *P–T* conditions where melt was reintegrated at 5 kbar and 797.94 °C.

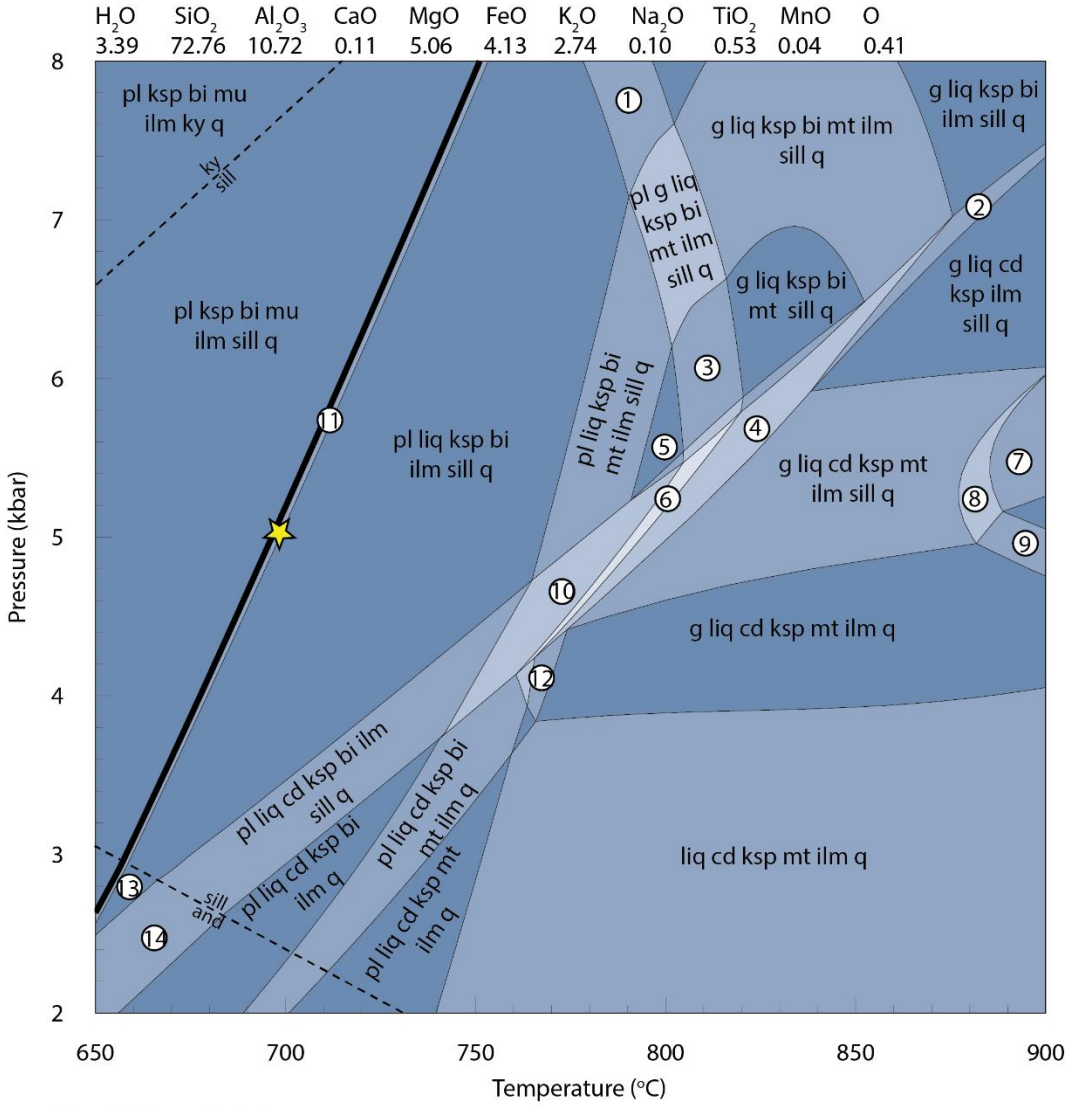

*Small fields not labelled

1. pl g liq ksp bi ilm sill q
2. g liq cd ksp bi ilm sill q
3. pl g liq ksp bi mt sill q
4. g liq cd ksp bi mt ilm sill q
5. pl liq ksp bi mt sill q
6. pl g liq cd ksp bi mt ilm sill q
7. g liq cd ksp sp ilm sill q
8. g liq cd ksp sp mt ilm sill q
9. g liq cd ksp sp mt ilm q
10. pl liq cd ksp bi mt ilm sill q
11. pl liq ksp bi mu ilm sill q
12. g liq cd ksp bi mt ilm q
13. pl liq ksp bi ilm and q
14. pl liq cd ksp bi ilm and q

Figure 11. Calculated *P–T* pseudosection after first melt reintegration (6% melt reintegrated).

The bulk composition (in mol%) was calculated with the addition of 6% melt into the original granulite composition (Figure 10) and is given above the pseudosection. The bold black line represents the solidus. The yellow star represents the *P–T* conditions where melt was reintegrated, at 5 kbar and 698.24 °C.

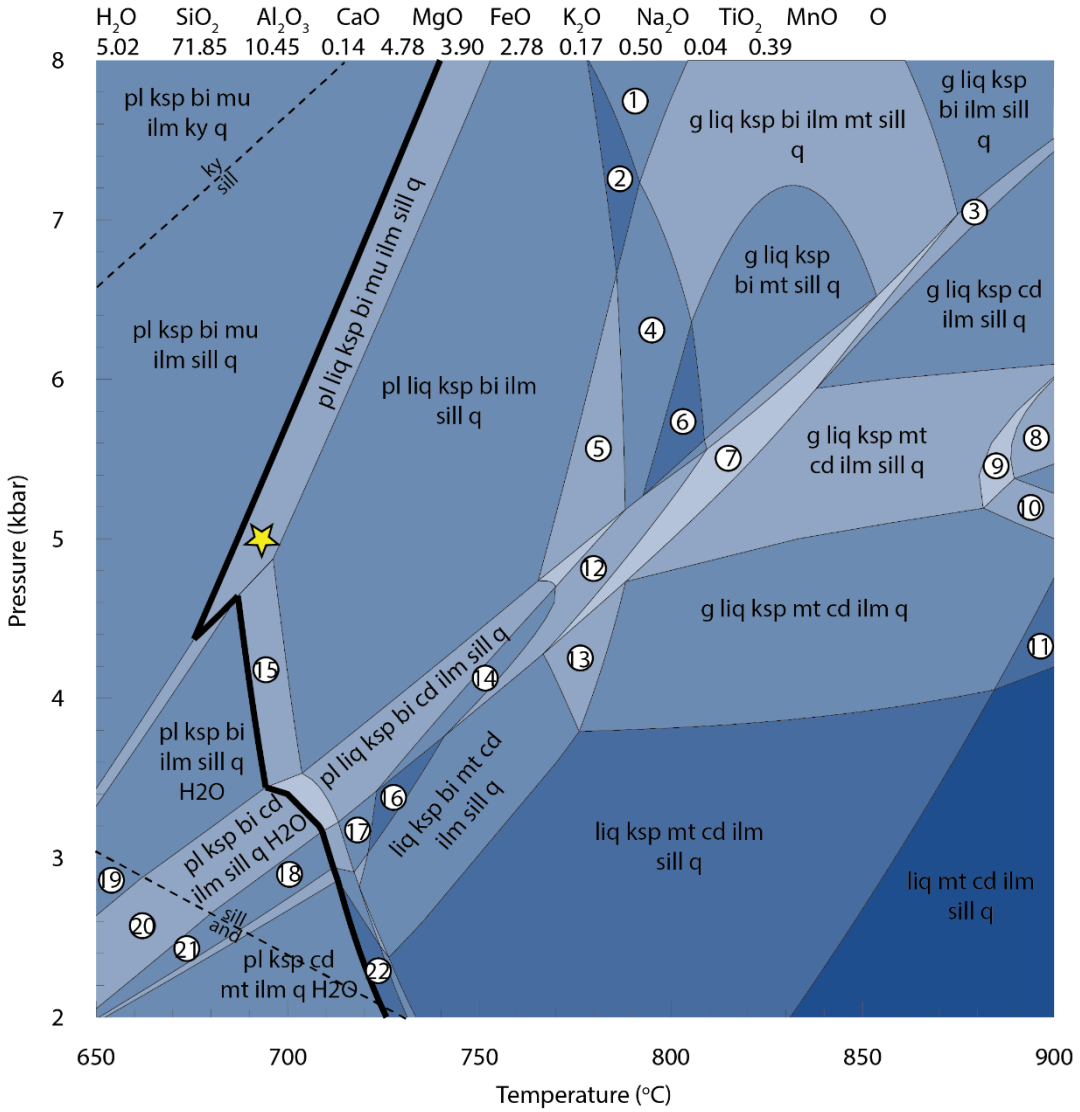

*Small fields not labelled

1. g liq ksp bi ilm sill q
2. liq ksp bi ilm sill q
3. g liq ksp bi cd ilm sill q
4. liq ksp bi ilm mt sill q
5. pl liq ksp bi mt ilm sill q
6. liq ksp bi mt sill q
7. g liq ksp bi mt cd ilm sill q
8. g liq ksp sp cd ilm sill q
9. g liq ksp mt sp cd ilm sill q
10. g liq ksp mt sp cd ilm q
12. g liq ksp bi mt cd ilm sill q
13. g liq ksp bi mt cd ilm q
14. liq ksp bi cd ilm sill q
15. pl liq ksp bi ilm sill q H2O
16. liq ksp bi cd ilm sill q
17. pl liq ksp bi cd ilm q
18. pl ksp bi cd ilm q H2O
19. pl ksp bi ilm and q H2O
20. pl ksp bi cd ilm and q H2O
21. pl ksp bi cd ilm q H2O
22. pl liq ksp cd mt ilm q H2O

Figure 12. Calculated *P–T* pseudosection after second melt reintegration (12% melt reintegrated).

The bulk composition (in mol%) was calculated with the addition of a further 6% melt into the first melt reintegration pseudosection (Figure 11) and is given above the pseudosection. The bold black line represents the solidus. The yellow star represents the *P–T* conditions where melt was reintegrated at 5 kbar and 690.11°C.

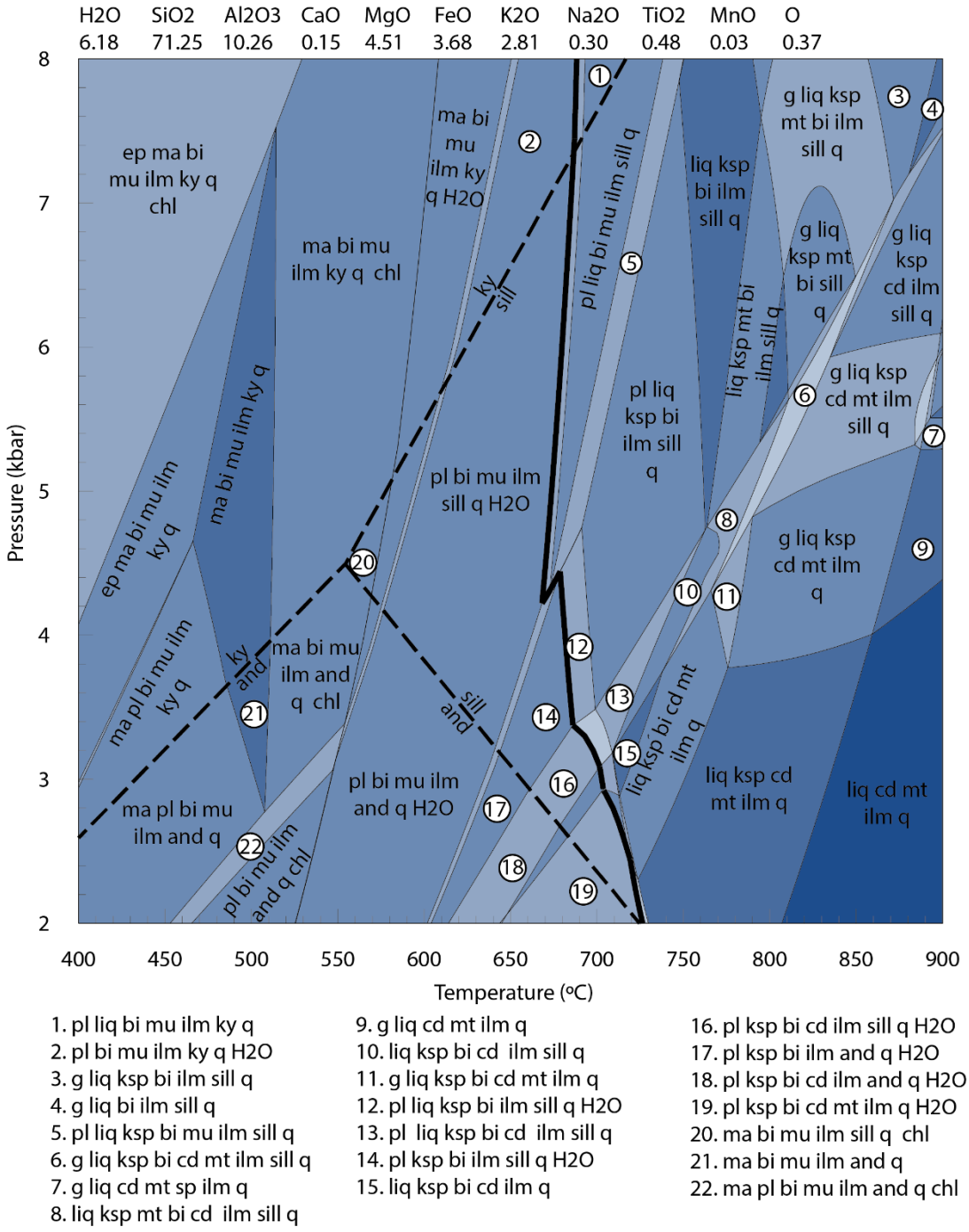

Figure 13. Calculated *P–T* pseudosection after third melt reintegration (18% melt reintegrated).

The bulk composition (in mol%) was calculated from the addition of a further 6% melt into the second melt reintegration pseudosection (Figure 12) and is given above the pseudosection. The bold black line represents the solidus.

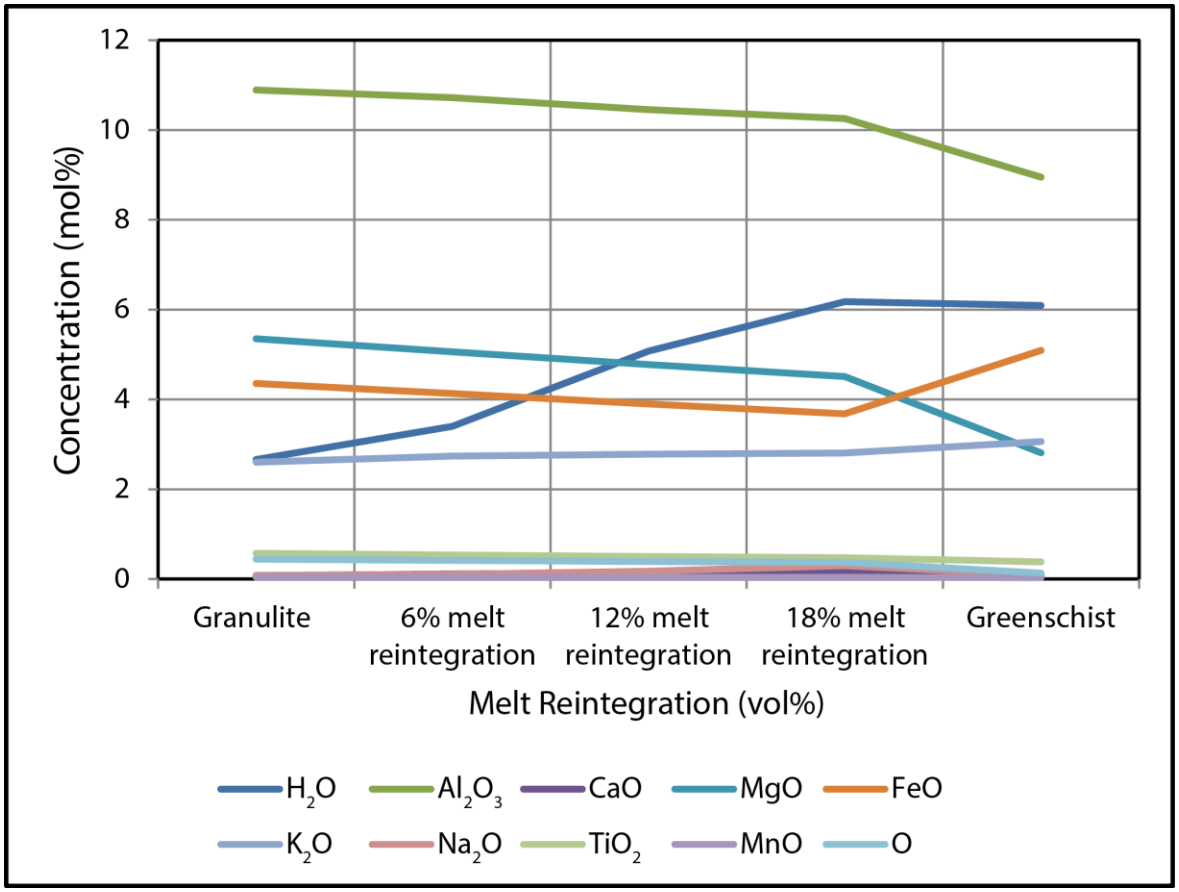

Figure 14. Changing element concentrations with progressive melt reintegration.

The average granulite bulk composition is given as a starting point and the average greenschist bulk composition as the end point.

5. DISCUSSION

The objective of this study is to compare the current models for melt loss and melt reintegration with a natural laboratory represented by the Pine Hill Formation within the Reynolds Range Group in central Australia. The Reynolds Range provides a continuous stratigraphic unit, along which compositions can be tracked and compared to calculated melt loss or reintegration models.

5.1. Limitations of the modelling

There are a number of limitations and caveats to the phase equilibria modelling discussed above. Some limitations relate to the models themselves, including the uncertainties associated with the internally consistent thermodynamic data and the activity-composition models used in THERMOCALC to calculate the phase equilibria models (Powell and

Holland 2008). The simplifications that are necessary to model phase equilibria diagrams in naturally complex chemical systems are also a limiting factor. The model chemical system used in this study does not take into account minor components, such as chlorine and fluorine in biotite (Peterson et al. 1991). Although the effects of these minor components are unlikely to greatly influence the outcomes of the modelling, they are real and will modify slight details of reactions in *P–T* space (White et al. 2007).

The proportion of FeO to Fe_2O_3 can greatly affect the stability of a number of oxides and silicates (Holland and Powell 2001, Boger et al. 2012, Morrissey et al. 2015). The samples used in this study were obtained from surface outcrops in central Australia, which is a naturally oxidised landscape and prevents an appropriate determination of the oxidation state by titration. While every effort was made to determine an oxidation state that was representative of the samples, some variation in the oxidation state may result in differences in the stability of some mineral assemblages. An additional and important caveat is that the bulk compositions used in the modelling are the average compositions taken from the greenschist and granulite traverses. This means that they do not relate to any specific rock sample, but rather are an attempt to understand the average response of the Pine Hill Formation to progressive metamorphism, partial melting and melt loss. This means that a determination of variables such as oxidation state based on the observed mineral assemblages are also limited.

The models are further limited by the simplifications of the *P–T* paths that were modelled. The consequences of melt loss modelling are shown in Figures 5–7. Melt loss events were calculated at a pressure of 5 kbar, based on a linear interpolation of the *P–T* stability of andalusite assemblages in the central Reynolds Range, and the computed *P–T* conditions in the easternmost Reynolds Range (Morrissey et al. 2014). However, cordierite is not stable

at pressures of 5 kbar, despite being part of the granulite facies peak assemblage (Figures 6, 7). Therefore, the peak pressure conditions in the Pine Hill Formation are likely to be closer to 4.5 kbar. This only became evident once the *P–T* modelling reached an advanced stage. Unfortunately given the project time constraints, it was not possible to complete a new series of melt loss models at a pressure of 4.5 kbar. However, as the modal contours for melt are steeply inclined in *P–T* space (e.g. Figure 7), and the compositions of melt at 4.5 and 5 kbar are similar, this does not significantly affect the discussion below.

5.2. Melt loss calculations

Melting of the Pine Hill Formation has converted a greenschist facies biotite–muscovite–chlorite–quartz±rutile±ilmenite assemblage into a biotite–sillimanite–cordierite–K-feldspar–quartz–magnetite–ilmenite–melt±garnet–bearing granulite. Figures 4–7 show the evolving modelled bulk rock composition as melt loss progressed.

For the incremental melt loss calculations in this study, melt was allowed to drain from the rock when its proportion equalled the melt connectivity transition (MCT) of 7 mol%. Strictly speaking, the MCT is purely a rheological transition and not a percolation threshold, as it represents the structural change in the crust with an increasing volume of melt in a static system (Rosenberg and Handy 2005). The actual percolation threshold for melt extraction in systems undergoing deformation is unknown, and is often thought to be lower than the MCT (Brown 2010). Therefore, this value was used as a reasonable upper boundary. Small variations in the melt percolation threshold have been found to make very little difference to the final outcome of melt loss or reintegration modelling (Korhonen et al. 2013). Different pressures and temperatures used for melt extraction within the same assemblage were also found to make little difference to the resulting composition,

suggesting that one of the strongest controls on melt composition is the assemblage in which the melt is generated (Korhonen et al. 2013).

The peak field of the average greenschist bulk composition is interpreted as a combination of the fields comprising ep–bi–mu–chl–q–H_2O±ru±ilm. Epidote is not observed in any of the samples, but the modal proportion of epidote in the interpreted peak fields is extremely low, meaning that epidote may not be present or is present in such small abundances that it would rarely be seen in the samples. It should also be noted that the modelled composition is an average of a number of samples from the greenschist facies Pine Hill Formation, and therefore is not specific to an individual sample.

In practise it is extremely difficult to track compositional changes associated with melting and melt loss in granulite terrains because only in very rare cases, such as in the Reynolds Range, can a single melt prone stratigraphic unit be traced from greenschist to granulite facies conditions. The incremental melt loss modelling of the protolith up to 18% along a simplified *P–T* trajectory did not produce the mineral assemblages that are observed in the granulite facies part of the Pine Hill Formation as was hypothesised. However, further *T–*M_O modelling (Figure 8) shows that the granulite mineral assemblages could be formed after 18% incremental melt loss for a slightly more oxidised composition. This variance between the actual oxidation state of the protolith bulk composition and that required to produce mineral assemblages observed in the granulite is likely a result of the variation in protolith compositions that were averaged for the initial greenschist composition.

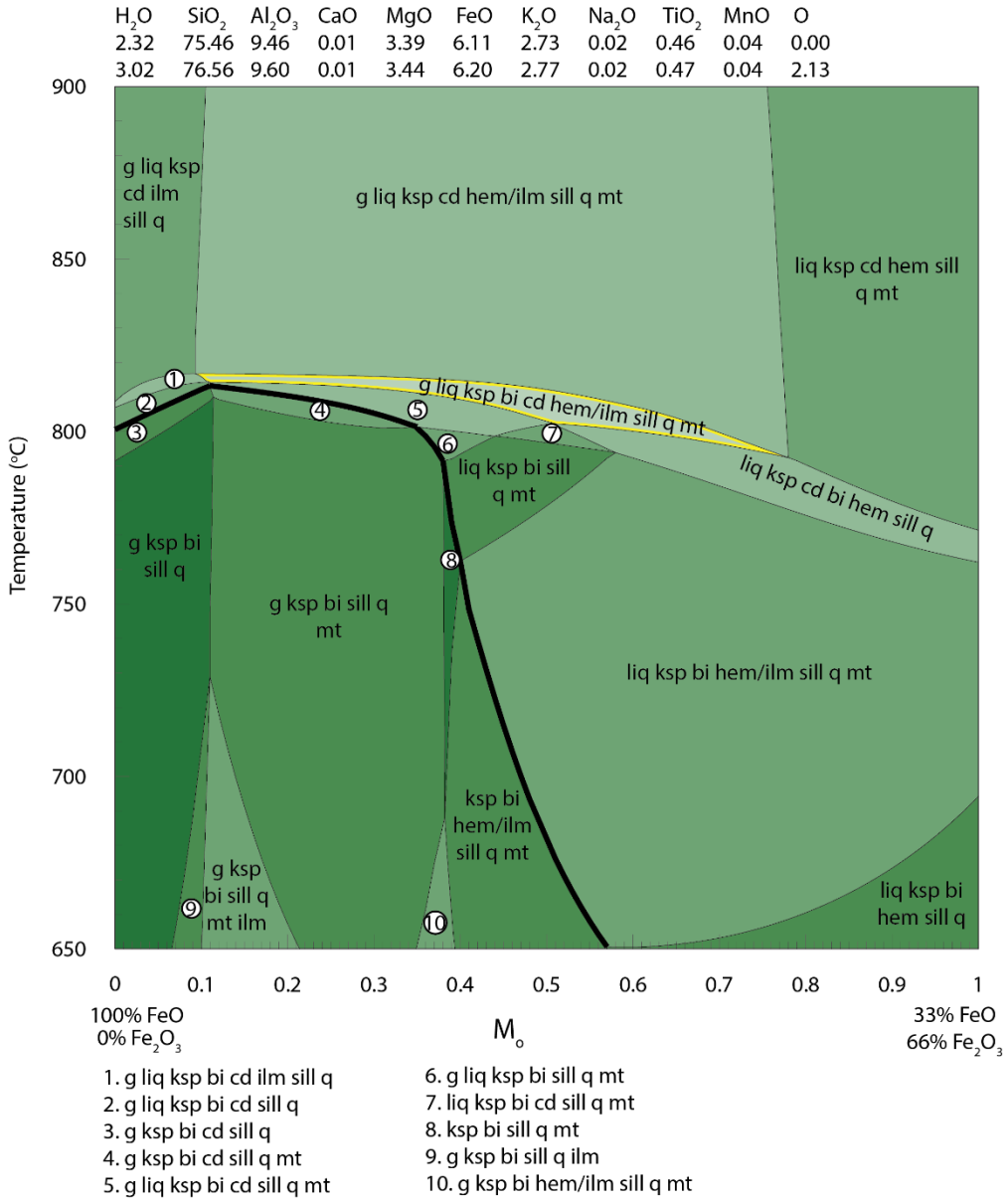

Figure 15. Calculated *T*–*M*O section after third stage melt loss.

The bulk compositions (in mol%) were calculated after third melt loss (Figure 7) at 5 kbar and are given on top of the pseudosection. The bold black line represents the solidus. The field g-liq-ksp-bi-cd-hem/ilm-sill-q-mt, outlined in yellow, represents the peak assemblage in some of the average granulite bulk composition.

Compositional changes during progressive melt loss include gradual increases in the concentrations of Al_2O_3, FeO, MgO, TiO_2, MnO and O, whereas the concentrations of H_2O, SiO_2, CaO, K_2O and Na_2O decrease. Some of these elements follow the expected trend of a terrain that is losing melt. However, the measured average granulite composition is significantly richer in Mg than can be plausibly explained by melt loss from the average greenschist composition unless the total volume of melt loss was much greater than what has been modelled. However, this would result in a FeO value far beyond what is observed

in the average granulite rock composition (Figure 10). Although every attempt was made to sample a representative average bulk composition of the greenschist and granulite facies parts of the Pine Hill Formation, it is evident that it is not possible to reconcile the FeO composition of the residual granulite with the composition that was modelled from the greenschist average bulk composition. This may suggest that the original protolith composition of the Pine Hill Formation was variable, and the part of the formation now at granulite grade was always less Fe-rich than the lower grade composition. Alternatively, it may be that despite attempting to obtain representative samples of the Pine Hill Formation, the computed averages are not accurate representations. In the north-west Reynolds Range the greenschist Pine Hill Formation is approximately 1 km wide, whereas in the granulite region it is approximately 700 m wide. In both instances the unit preserves centimetre-to-metre scale relict sedimentary bedding and the outcrop is not continuous. The choice of samples for geochemical analyses was an assessment made in the field, and therefore the weighting of samples chosen may not be representative of the overall compositions, particularly at the granulite, where the outcrop was discontinuous. Both of these factors make determining a representative composition difficult.

5.2.1. CATASTROHPIC VERSUS INCREMENTAL MELT LOSS CALCULATIONS

In deforming terrains such as that now exposed in the Reynolds Range, melting is generally considered to be an open system process in which melt is lost gradually from melt fertile rocks (Sawyer 1994, Brown 2007, Yakymchuk and Brown 2014a). Melt loss requires the establishment of a percolation threshold, which although poorly understood, has been considered to be effectively established when melt reaches 7 mol% (*c.* 7 vol%) of the total volume (Rosenberg and Handy 2005). Once a percolation threshold has been established, melt loss is considered to be possible via a grain boundary migration process (Brown 2010, Brown 2013), enhanced by deformation (Korhonen et al. 2013), with a small

amount of melt remaining (~1 mol%) after draining has occurred (Sawyer 2001, Holness and Sawyer 2008). However, if the rate of melt generation greatly exceeds the rate of melt loss, either because of rock fertility, the rate of heating or the presence of melt impermeable layers oriented at a high angle to the direction of melt migration (e.g. Hand and Dirks 1992, Thompson and Connolly 1995, Snelling 2008), melt will build up until catastrophic and potentially structurally destructive rapid melt migration occurs (e.g. Gardien et al. 1995, Davies and Tommasini 2000, Miyazaki 2007).

Further to the incremental melt loss calculations above, the same average greenschist composition was used to calculate melt loss compositions for comparison (Figure 9, Appendix 5) in the situation where melt was able to build up well beyond the percolation threshold. After 18% melt loss, there were no significant differences between the incremental composition and the catastrophic composition for this system, meaning that the bulk chemistry alone cannot be used as a definitive way to determine the mode of melt loss.

Highly silicious compositions often result in few, large fields at high temperatures (e.g. Kelsey et al. 2005); meaning that few phases change over large temperature ranges. As one of the major controls on melt composition is the mineral assemblage in which melt is generated (Korhonen et al. 2013), the small number of changes that occur above the solidus in this protolith composition (Figure 4) may be the reason for the similarity between the final compositions of incremental and catastrophic melt loss. Further incremental melt loss modelling would be needed to truly compare the two in this situation. A greater difference between incremental and catastrophic melt loss modelling compositions may be observed in more sensitive bulk compositions, where more mineral reactions occur over a narrower temperature range.

Calculations for the case of catastrophic melt loss did not reveal any conclusive results on the total volume of melt that was removed from the system during metamorphism. Figure 9 shows the trends of each element at each volume of melt loss, with the greenschist and granulite compositions included for comparison. Most elements appear to have been depleted or enriched too far after 55% melt loss, indicating that this value is likely an upper limit.

5.2.2. MELT FERTILITY

In the context presented here, the fertility of a rock refers to its ability to generate melt. The effect of melt loss is to reduce the fertility of a rock by removing the components that facilitate melting, and therefore incremental melt loss should result in a progressively less fertile composition that produces less melt than the precursor composition (e.g. Douce and Johnston 1991, Singh and Manglik 2000). The fertility of the open system in this study in comparison to the closed system was assessed by calculating the volume of melt that would be produced along an isobaric *P–T* path at 5 kbar. Figure 16 shows the difference in melt fertility between the open and closed systems.

The fertility of the closed system is greater than that of the open system after its first melt loss event (6 % melt loss). However, the fertility of the open system after it has lost 12% melt is briefly greater than the closed system at the same *P–T* conditions. With larger amounts of melt loss, the open system is less fertile than the closed system (Figure 16).

In both systems, melt is primarily produced during the muscovite and biotite breakdown reactions (Clemens and Vielzeuf 1987, White and Powell 2002). The open system briefly produces more melt than the closed system at approximately 720 °C, as shown in Figure

16. This may be due to stabilisation of muscovite to higher temperatures in the open system (Figures 4, 10), allowing the muscovite breakdown reaction to continue to higher temperatures in the open system and temporarily produce more melt.

Biotite is still stable at 800 °C but the difference in fertility could not be investigated at higher temperatures without further melt loss modelling, which was not possible due to time constraints. However, the reconnaissance calculations suggest that the difference in melt produced by each system will increase as the open system becomes increasingly H_2O depleted and more residual.

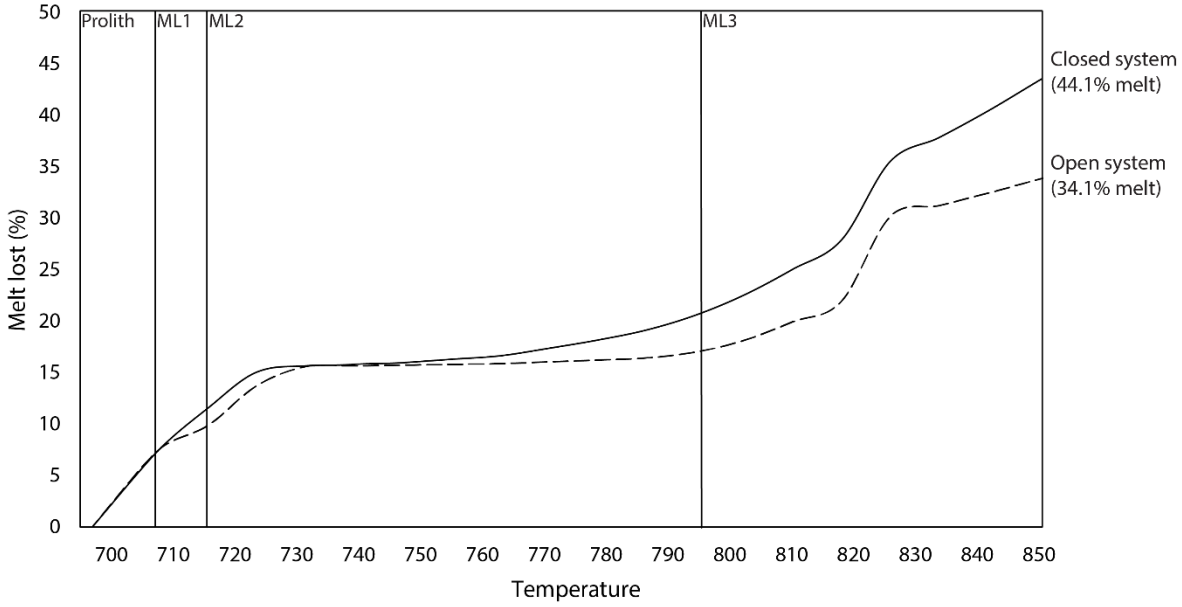

Figure 16. Difference in melt fertility between the open system and the closed system.

Each vertical line represents a new composition in the open system (ML1 = Melt Loss 1, ML2 = Melt Loss 2, ML3 = Melt Loss 3). All calculations for the closed system were done with the protolith composition.

5.2.3. STRUCTURAL CONTROLS ON THE STYLE OF MELT LOSS

Whether melt is lost incrementally or catastrophically is largely dependent on the structural setting and the lithologies surrounding the melt fertile layer (Brown 2007). The granulite of the Pine Hill Formation shows excellent preservation of relict sedimentary layering (Figure 2g), even though melt has clearly been lost. This suggests that melt probably left in small

batches that did not disrupt the layering. However, a single, large-scale melt loss event may have been possible while still maintaining the integrity of the sedimentary layering. Melt will remain in a closed system until a percolation threshold is reached and it is structurally able to leave (Singh and Manglik 2000, Rosenberg and Handy 2005). However, lithologies such as marble and calc-silicates may act as barriers that prevent the melt from leaving; resulting in a build-up of melt in melt prone units (Hand and Dirks 1992). The pelitic granulite in the Pine Hill Formation is stratigraphically bound by marbles and calc-silicates belonging to the Upper Calc-Silicate unit of the Reynolds Range Group (Dirks 1990). Hand and Dirks (1992) showed that similar lithologies elsewhere in the Reynolds Range Group acted as effective barriers to migration of melt derived from felsic gneisses. If melt impermeable units exist within the stratigraphy, melt could have accumulated until a suitable structural trigger facilitated melt migration. Within the Reynolds Range Group, one obvious trigger was the development of the upright isoclinal folds (Dirks and Wilson 1990) that rotated the stratigraphy from sub horizontal with the Upper Calc-Silicate sitting above the Pine Hill Formation, to sub-vertical. This would have effectively removed the Upper Calc-Silicate as a barrier to melt migration, allowing melt to migrate upwards through the Pine Hill Formation. Melt migration may have then been triggered by folding, which rotated the melt-impermeable units from shallowly dipping to their current sub-vertical orientation. This may have allowed the melt to migrate through the fold limbs in reasonably high volumes, without overly disturbing the original layering.

5.3. Melt reintegration calculations

An alternative way to evaluate the modelling of melt loss in granulites is to reintegrate melt into the residual granulite composition. Melt reintegration is a fundamentally different problem to melt loss and is the situation that petrologists most commonly face. Melt reintegration is generally an attempt to reconstruct a viable protolith composition in which

the minerals observed in the residuum grew, so that a prograde path can be constructed and assessed. Reconstruction of a plausible bulk composition for the protolith requires melt with a composition that is in equilibrium with the residual composition at a given pressure and temperature, to be reintegrated via a series of down temperature steps (e.g. White et al. 2004, Diener et al. 2008, Korhonen et al. 2013).

Figures 10–13 show the progressive change in the modelled composition of the granulite as melt is added back into the progressively less residual composition. The *P–T* model produced for the third melt reintegration (Figure 13) has some similarities to the greenschist model (Figure 4). A water saturated solidus is reproduced and K-feldspar becomes stable at low pressures below the solidus. However, many low-temperature sub-solidus fields could not be reproduced, including the interpreted peak field in the greenschist. The aluminosilicate minerals (kyanite–sillimanite–andalusite) have a much wider stability range in the melt reintegrated model, potentially due to its higher aluminium concentration. The H_2O content in the melt reintegrated model is also likely to be lower than in the original greenschist facies composition, as reintegrating melt does not allow for a consideration of subsolidus prograde dehydration reactions. As H_2O was set to excess in the greenschist model, but not in the melt reintegration model, this may have implications for the stability of some sub-solidus minerals (Webb et al. 2015). Compositionally, melt reintegration modelling resulted in a protolith composition that was somewhat similar to the actual protolith, but could not reproduce the observed peak assemblage. This could potentially be due to sampling and compositional errors, or alternatively may indicate that more melt would need to be reintegrated to reach the final composition. This demonstrates the limitations and uncertainties involved with melt reintegration modelling on rocks with unknown protoliths.

5.4. Implications for metamorphic induced differentiation of crustal heat production

The results of melt loss modelling in the Pine Hill Formation show that the observed peak metamorphic assemblages can be produced with approximately 18% melt loss. Appendix 1 shows a comparison of KUTh concentrations and crustal heat production rates determined by calibrated gamma ray spectrometry along several traverses of increasing grade in the Pine Hill Formation (see Appendix 1 for details of this part of the project). It is evident that despite significant melt loss in the granulites, the overall crustal heat production rate is slightly higher than the greenschist region. This is because while K and the much more thermally energetic U have been reduced in the granulites, the concentration of Th was not.

The consequence of retaining similar heat production rates is that the granulitic rocks of the Pine Hill Formation remained thermally energetic, despite approximately 18% melt loss. The pattern of metamorphic isograds in the Reynolds Range region generated during the 400–320 Ma Alice Springs Orogeny is essentially identical to the pattern of isograds associated with the 1600–1530 Ma Chewings Event that produced the granulites (Hand and Buick 2001). This suggests that the elevated levels of crustal heat production that were likely to have driven the Chewings-aged metamorphism (Sandiford and Hand 1998, Anderson et al. 2013, Morrissey et al. 2014) were sufficiently preserved to also drive the early Palaeozoic Alice Springs Orogeny metamorphism.

6. CONCLUSIONS

Partial melting and melt loss associated with granulite facies metamorphism can greatly affect the rheology, composition and long-term thermal character of the crust, defining how residual terrains will respond to future tectonic processes. Phase equilibria modelling highlights the importance of melt loss in forming depleted, residual granulite terrains.

Unfortunately, the weighting of samples used to obtain the bulk greenschist and granulite compositions of Pine Hill Formation for this study were not completely representative. However, the results presented here do show that the Pine Hill Formation was likely to have lost approximately 18% melt through metamorphism from greenschist to granulite facies, although whether it was through a single catastrophic event or many small incremental losses remains uncertain. Open system melting resulted in a composition that was less fertile than the closed system. Melt loss resulted in the slight concentration of KUTh in the residuum relative to the protolith, suggesting that metamorphic processes may not be responsible for the depletion of these heat producing elements. The inability to reach the interpreted peak assemblage of the greenschist from melt reintegration modelling from the granulite composition demonstrates the uncertainties and risks associated with inverse modelling.

7. ACKNOWLEDGMENTS

Supervisors Martin Hand, Dave Kelsey and Karin Barovich are thanked for their continued support and guidance. Ben Wade, Adelaide Microscopy is thanked for assistance with SEM imaging and electron microprobe analyses. Laura Morrissey and Naomi Tucker are thanked for their generous and invaluable assistance with THERMOCALC modelling.

REFERENCES

ANDERSON J. R., KELSEY D. E., HAND M. & COLLINS W. J. 2013. Conductively driven, high-thermal gradient metamorphism in the Anmatjira Range, Arunta region, central Australia. *Journal of Metamorphic Geology* **31**, 1003-1026.

ANDREOLI M. A., HART R. J., ASHWAL L. D. & COETZEE H. 2006. Correlations between U, Th content and metamorphic grade in the western Namaqualand Belt, South Africa, with implications for radioactive heating of the crust. *Journal of Petrology* **47**, 1095-1118.

AREVALO JR R., MCDONOUGH W. F. & LUONG M. 2009. The K/U ratio of the silicate Earth: Insights into mantle composition, structure and thermal evolution. *Earth and Planetary Science Letters* **278**, 361-369.

BEA F. 1996. Residence of REE, Y, Th and U in granites and crustal protoliths; implications for the chemistry of crustal melts. *Journal of Petrology* **37**, 521-552.

BEA F. & MONTERO P. 1999. Behavior of accessory phases and redistribution of Zr, REE, Y, Th and U during metamorphism and partial melting of metapelites in the lower crust: an example from the Kinzigite Formation of Ivrea-Verbano, NW Italy. *Geochimica et Cosmochimica Acta* **63**, 1133-1153.

BEA F. 2012. The sources of energy for crustal melting and the geochemistry of heat-producing elements. *Lithos* **153**, 278-291.

BOGER S. D., WHITE R. W. & SCHULTE B. 2012. The importance of iron speciation (Fe+2/Fe+3) in determining mineral assemblages: an example from the high-grade aluminous metapelites of southeastern Madagascar. *Journal of Metamorphic Geology* **30**, 997-1018.

BROWN M. 1994 Melt segregation mechanism controls on the geochemistry of crustal melts. VM Goldschmidt Conference, Mineralogical Magazine A. pp. 124-125.

BROWN M. & SOLAR G. S. 1998. Shear-zone systems and melts: feedback relations and self-organization in orogenic belts. *Journal of Structural Geology* **20**, 211-227.

BROWN M. 2007. Crustal melting and melt extraction, ascent and emplacement in orogens: mechanisms and consequences. *Journal of the Geological Society* **164**, 709-730.

BROWN M. 2010. The spatial and temporal patterning of the deep crust and implications for the process of melt extraction. *Philosophical Transactions: Mathematical, Physical and Engineering Sciences* **368**, 11-51.

BROWN M. 2013. Granite: From genesis to emplacement. *Geological Society of America Bulletin* **125**, 1079-1113.

BUCHER K. & GRAPES R. 2011 Metamorphism of Pelitic Rocks (Metapelites). Petrogenesis of Metamorphic Rocks. pp. 257-313. Springer Berlin Heidelberg.

BUICK I. S., FREI R. & CARTWRIGHT I. 1999. The timing of high-temperature retrogression in the Reynolds Range, central Australia: constraints from garnet and epidote Pb-Pb dating. *Contributions to Mineralogy and Petrology*` **135**, 244-254.

CARTWRIGHT I., BUICK I., FOSTER D. & LAMBERT D. 1999. Alice Springs age shear zones from the southeastern Reynolds Range, central Australia. *Australian Journal of Earth Sciences* **46**, 355-363.

CLAOUÉ-LONG J., EDGOOSE C. & WORDEN K. 2008. A correlation of Aileron Province stratigraphy in central Australia. *Precambrian Research* **166**, 230-245.

CLARKE G. L. & POWELL R. 1991. Proterozoic granulite facies metamorphism in the southeastern Reynolds Range, central Australia: geological context, P–T path and overprinting relationships. *Journal of Metamorphic Geology* **9**, 267-281.

CLEMENS J. & VIELZEUF D. 1987. Constraints on melting and magma production in the crust. *Earth and Planetary Science Letters* **86**, 287-306.

COLLINS W. J. & VERNON R. H. 1991. Orogeny associated with anticlockwise P-T-t paths: evidence from low-P, high-T metamorphic terranes in the Arunta inlier, central Australia. *Geology* **19**, 835-838.

COLLINS W. J. & WILLIAMS I. S. 1995. SHRIMP ionprobe dating of short-lived Proterozoic tectonic cycles in the northern Arunta Inlier, central Australia. *Precambrian Research* **71**, 69-89.

DAVIES G. R. & TOMMASINI S. 2000. Isotopic disequilibrium during rapid crustal anatexis: implications for petrogenetic studies of magmatic processes. *Chemical Geology* **162**, 169-191.

DIENER J. F. A., WHITE R. W. & POWELL R. 2008. Granulite facies metamorphism and subsolidus fluid-absent reworking, Strangways Range, Arunta Block, central Australia. *Journal of Metamorphic Geology* **26**, 603-622.

DIRKS P. 1990. Intertidal and subtidal sedimentation during a mid-Proterozoic marine transgression, reynolds range group, Arunta block, central Australia. *Australian Journal of Earth Sciences* **37**, 409-422.

DIRKS P. & WILSON C. J. L. 1990. The geological evolution of the Reynolds Range, central Australia - evidence for 3 distinct structural-metamorphic cycles. *Journal of Structural Geology* **12**, 651-665.

DOUCE A. E. P. & JOHNSTON A. D. 1991. Phase equilibria and melt productivity in the pelitic system: implications for the origin of peraluminous granitoids and aluminous granulites. *Contributions to Mineralogy and Petrology* **107**, 202-218.

ENGLAND P. C. & THOMPSON A. B. 1984. Pressure—temperature—time paths of regional metamorphism I. Heat transfer during the evolution of regions of thickened continental crust. *Journal of Petrology* **25**, 894-928.

FOERSTER H. J. & HARLOV D. E. 1999. Monazite-(Ce)-huttonite solid solutions in granulite-facies metabasites from the Ivrea-Verbano Zone, Italy. *Mineralogical Magazine* **63**, 587-594.

GARDIEN V., THOMPSON A. B., GRUJIC D. & ULMER P. 1995. Experimental melting of biotite+ plagioclase+ quartz±muscovite assemblages and implications for crustal melting. *Journal of Geophysical Research: Solid Earth (1978–2012)* **100**, 15581-15591.

HAND M. & DIRKS P. H. G. M. 1992. The influence of deformation on the formation of axial-planar leucosomes and the segregation of small melt bodies within the migmatitic Napperby Gneiss, central Australia. *Journal of Structural Geology* **14**, 591-604.

HAND M. & BUICK I. S. 2001 Tectonic evolution of the Reynolds-Anmatjira Ranges: a case study in terrain reworking from the Arunta Inlier, central Australia. *In* MILLER J.*, et al.* eds. Continental Reactivation and Reworking. pp. 237-260.

HANSON R. B. & BARTON M. D. 1989. Thermal development of low-pressure metamorphic belts: Results from two-dimensional numerical models. *Journal of Geophysical Research: Solid Earth (1978–2012)* **94**, 10363-10377.

HOLLAND T. I. M. & POWELL R. 2001. Calculation of Phase Relations Involving Haplogranitic Melts Using an Internally Consistent Thermodynamic Dataset. *Journal of Petrology* **42**, 673-683.

HOLLAND T. J. B. & POWELL R. 2011. An improved and extended internally consistent thermodynamic dataset for phases of petrological interest, involving a new equation of state for solids. *Journal of Metamorphic Geology* **29**, 333-383.

HOLNESS M. B. & SAWYER E. W. 2008. On the Pseudomorphing of Melt-filled Pores During the Crystallization of Migmatites. *Journal of Petrology* **49**, 1343-1343.

HOWLETT D., RAIMONDO T. & HAND M. In Press. Evidence for 1808–1770 Ma bimodal magmatism, sedimentation, high temperature deformation and metamorphism in the Aileron Province, central Australia. *Australian Journal of Earth Sciences*.

JOHNSON T. E., BROWN M. & SOLAR G. S. 2003. Low–pressure subsolidus and suprasolidus phase equilibria in the MnNCKFMASH system: Constraints on conditions of regional metamorphism in western Maine, northern Appalachians. *American Mineralogist* **88**, 624-638.

JOHNSON T. E., WHITE R. W. & POWELL R. 2008. Partial melting of metagreywacke: a calculated mineral equilibria study. *Journal of Metamorphic Geology* **26**, 837-853.

JOHNSON T. E. & WHITE R. W. 2011. Phase equilibrium constraints on conditions of granulite-facies metamorphism at Scourie, NW Scotland. *Journal of the Geological Society* **168**, 147-158.

JOHNSON T. E., WHITE R. W. & BROWN M. 2011. A year in the life of an aluminous metapelite xenolith—The role of heating rates, reaction overstep, H2O retention and melt loss. *Lithos* **124**, 132-143.

KELSEY D. E., WHITE R. W. & POWELL R. 2005. Calculated phase equilibria in K2O-FeO-MgO-Al2O3-SiO2-H2O for silica-undersaturated sapphirine-bearing mineral assemblages. *Journal of Metamorphic Geology* **23**, 217-239.

KELSEY D. E., CLARK C. & HAND M. 2008. Thermobarometric modeling of zircon and monazite growth in melt-bearing systems: examples using model metapelitic and metapsammitic granulites. *Journal of Metamophic Geology* **26**, 199-212.

KORHONEN F. J., BROWN M., CLARK C. & BHATTACHARYA S. 2013. Osumilite–melt interactions in ultrahigh temperature granulites: phase equilibria modelling and implications for the P–T–t evolution of the Eastern Ghats Province, India. *Journal of Metamorphic Geology* **31**, 881-907.

LO PÒ D. & BRAGA R. 2014. Influence of ferric iron on phase equilibria in greenschist facies assemblages: the hematite-rich metasedimentary rocks from the Monti Pisani (Northern Apennines). *Journal of Metamorphic Geology* **32**, 371-387.

MARESCHAL J.-C. & JAUPART C. 2013. Radiogenic heat production, thermal regime and evolution of continental crust. *Tectonophysics*.

MIYAZAKI K. 2007. Formation of a high-temperature metamorphic complex due to pervasive melt migration in the hot crust. *Island Arc* **16**, 69-82.

MORRISSEY L. J., HAND M., RAIMONDO T. & KELSEY D. E. 2014. Long-lived high-T, low-P granulite facies metamorphism in the Arunta Region, central Australia. *Journal of Metamorphic Geology* **32**, 25-47.

MORRISSEY L. J., HAND M. & KELSEY D. E. 2015. Multi-stage metamorphism in the Rayner–Eastern Ghats Terrane: P–T–t constraints from the northern Prince Charles Mountains, east Antarctica. *Precambrian Research* **267**, 137-163.

OXBURGH E. 1980. Heat flow and magma genesis. *Physics of magmatic processes*, 161-199.

PETERSON J. W., CHACKO T. & KUEHNER S. M. 1991. The effects of fluorine on the vapor-absent melting of phlogopite + quartz; implications for deep-crustal processes. *American Mineralogist* **76**, 470-476.

POWELL R. & HOLLAND T. J. B. 1988. An internally consistent dataset with uncertainties and correlations: 3. Applications to geobarometry, worked examples and a computer program. *Journal of Metamorphic Geology* **6**, 173-204.

POWELL R. & HOLLAND T. J. B. 2008. On thermobarometry. *Journal of Metamorphic Geology* **26**, 155-179.

POWELL R., WHITE R. W., GREEN E. C. R., HOLLAND T. J. B. & DIENER J. F. A. 2014. On parameterizing thermodynamic descriptions of minerals for petrological calculations. *Journal of Metamorphic Geology* **32**, 245-260.

RAIMONDO T., CLARK C., HAND M. & FAURE K. 2011. Assessing the geochemical and tectonic impacts of fluid–rock interaction in mid-crustal shear zones: a case study from the intracontinental Alice Springs Orogen, central Australia. *Journal of Metamorphic Geology* **29**, 821-850.

RAPP R. P., WATSON E. B. & MILLER C. F. 1991. Partial melting of amphibolite/eclogite and the origin of Archean trondhjemites and tonalites. *Precambrian Research* **51**, 1-25.

RIGBY M. J. & DROOP G. T. R. 2011. Fluid-absent melting versus CO2 streaming during the formation of pelitic granulites: A review of insights from the cordierite fluid monitor. *Geological Society of America Memoirs* **207**, 39-60.

ROSENBERG C. L. & HANDY M. R. 2005. Experimental deformation of partially melted granite revisited: implications for the continental crust. *Journal of Metamorphic Geology* **23**, 19-28.

RUBATTO D., WILLIAMS I. S. & BUICK I. S. 2001. Zircon and monazite response to prograde metamorphism in the Reynolds Range, central Australia. *Contributions to Mineralogy and Petrology* **140**, 458-468.

RUDNICK R. L., MCLENNAN S. M. & TAYLOR S. R. 1985. Large ion lithophile elements in rocks from high-pressure granulite facies terrains. *Geochimica et Cosmochimica Acta* **49**, 1645-1655.

RUDNICK R. L. & FOUNTAIN D. M. 1995. Nature and composition of the continental crust: a lower crustal perspective. *Reviews Of Geophysics* **33**, 267-309.

SANDIFORD M. & HAND M. 1998. Controls on the locus of intraplate deformation in central Australia. *Earth and Planetary Science Letters* **162**, 97-110.

SANDIFORD M., HAND M. & MCLAREN S. 2001 Tectonic feedback, intraplate orogeny and the geochemical structure of the crust: a central Australian perspective. *In* MILLER J.*, et al.* eds. Polyphase tectonism and reactivation mechanisms in metamorphic belts*.* London: Geological Society of London.

SANDIFORD M., MCLAREN S. & NEUMANN N. 2002. Long-term thermal consequences of the redistribution of heat-producing elements associated with large-scale granitic complexes. *Journal of Metamorphic Geology* **20**, 87-98.

SANTOSH M., JACKSON D. H. & HARRIS N. B. W. 1993. The Significance of Channel and Fluid-Inclusion CO2 in Cordierite: Evidence from Carbon Isotopes. *Journal of Petrology* **34**, 233-258.

SAWYER E. 1994. Melt segregation in the continental crust. *Geology* **22**, 1019-1022.

SAWYER E. W. 2001. Melt segregation in the continental crust: distribution and movement of melt in anatectic rocks. *Journal of Metamorphic Geology* **19**, 291-309.

SCRIMGEOUR I. 2013 Ch. 12 Aileron Province. Geology and mineral resources of the Northern Territory*.* pp. 1-75. Northern Territory Geological Survey, Special Publications 5.

SIGHINOLFI G. P. 1971. Investigations into deep crustal levels: Fractionating effects and geochemical trends related to high-grade metamorphism. *Geochimica et Cosmochimica Acta* **35**, 1005-1021.

SINGH R. N. & MANGLIK A. 2000. Identification of radiogenic heat source distribution in the crust: A variational approach. *Sadhana* **25**, 111-118.

SNELLING A. A. 2008. Catastrophic granite formation: Rapid melting of source rocks and rapid magma intrusion and cooling. *Answers Research Journal* **1**, 11-25.

STEPANOV A. S., HERMANN J., RUBATTO D. & RAPP R. P. 2012. Experimental study of monazite/melt partitioning with implications for the REE, Th and U geochemistry of crustal rocks. *Chemical Geology* **300**, 200-220.

STEWART A. J., OFFE L. A., GLIKSON A. Y., JORRITSMA P. J. & PILINGER D. M. 1981 Geology of the Reynolds Range Region, Northern Territory 1:100 000 scale. 1st edition ed. Australia: Bureau of Mineral Resources.

THOMPSON A. B. & CONNOLLY J. A. 1995. Melting of the continental crust: some thermal and petrological constraints on anatexis in continental collision zones and other tectonic settings. *Journal of Geophysical Research: Solid Earth (1978–2012)* **100**, 15565-15579.

TURCOTTE D. L. & SCHUBERT G. 2002 Geodynamics. (2nd Edition edition). Cambridge, Cambridge.

VRY J., COMPSTON W. & CARTWRIGHT I. 1996. SHRIMP II dating of zircons and monazites: Reassessing the timing of high-grade metamorphism and fluid flow in the Reynolds Range, northern Arunta Block, Australia. *Journal of Metamorphic Geology* **14**, 335-350.

VRY J. K. & BAKER J. A. 2006. LA-MC-ICPMS Pb–Pb dating of rutile from slowly cooled granulites: Confirmation of the high closure temperature for Pb diffusion in rutile. *Geochimica Et Cosmochimica Acta* **70**, 1807-1820.

WEBB G., POWELL R. & MCLAREN S. 2015. Phase equilibria constraints on the melt fertility of crustal rocks: the effect of subsolidus water loss. *Journal of Metamorphic Geology* **33**, 147-165.

WHITE, POWELL, HOLLAND & WORLEY 2000. The effect of TiO2 and Fe2O3 on metapelitic assemblages at greenschist and amphibolite facies conditions: mineral equilibria calculations in the system K2O–FeO–MgO–Al2O3–SiO2–H2O–TiO2–Fe2O3. *Journal of Metamorphic Geology* **18**, 497-511.

WHITE R. & POWELL R. 2002. Melt loss and the preservation of granulite facies mineral assemblages. *Journal of Metamorphic Geology* **20**, 621-632.

WHITE R. W., POWELL R. & HOLLAND T. J. B. 2001. Calculation of partial melting equilibria in the system Na2O-CaO-K2O-FeO-MgO-Al2O3-SiO2-H2O (NCKFMASH). *Journal of Metamorphic Geology* **19**, p.139.

WHITE R. W., POWELL R. & HALPIN J. A. 2004. Spatially-focussed melt formation in aluminous metapelites from Broken Hill, Australia. *Journal of Metamorphic Geology* **22**, 825-845.

WHITE R. W., POWELL R. & HOLLAND T. J. B. 2007. Progress relating to calculation of partial melting equilibria for metapelites. *Journal of Metamorphic Geology* **25**, 511-527.

WHITE R. W., POWELL R., HOLLAND T. J. B., JOHNSON T. E. & GREEN E. C. R. 2014a. New mineral activity–composition relations for thermodynamic calculations in metapelitic systems. *Journal of Metamorphic Geology* **32**, 261-286.

WHITE R. W., POWELL R. & JOHNSON T. E. 2014b. The effect of Mn on mineral stability in metapelites revisited: new a–x relations for manganese-bearing minerals. *Journal of Metamorphic Geology* **32**, 809-828.

WORDEN K. E., CARSON C. J., CLOSE D. F., DONNELLAN N. & SCRIMGEOUR I. S. 2008 Summary of Results. Joint NTGS-GA geochronology: Tanami Region, Arunta Region, Pine Creek Orogen and Halls Creek Orogen correlatives, January 2005-March 2007. Northern Territory Geological Survey Record 2008-003.

YAKYMCHUK C. & BROWN M. 2014a. Behaviour of zircon and monazite during crustal melting. *Journal of the Geological Society* **171**, 465-479.

YAKYMCHUK C. & BROWN M. 2014b. Consequences of open-system melting in tectonics. *Journal of the Geological Society* **171**, 21-40.

ZULUAGA C. A., STOWELL H. H. & TINKHAM D. K. 2005. The effect of zoned garnet on metapelite pseudosection topology and calculated metamorphic P-T paths. *American Mineralogist* **90**, 1619-1628.

APPENDIX 1: HEAT PRODUCTION

Metamorphism involving partial melting is a fundamental process leading to the geochemical differentiation of Earth's crust. A primary expression of this process is the formation of granites that contain a component of crust within them, and the generation of granulite-facies metamorphic rocks that reflect the residuum left behind after extraction of granitic melts. It is known that granites are typically enriched in the heat producing elements (HPEs) K–U–Th, so it stands to reason that residual granulites are depleted in those elements (Rudnick and Fountain 1995, Bea 2012, Mareschal and Jaupart 2013). This has been a long standing premise for the way in which heat generation is distributed in the crust (e.g. Figure 3).

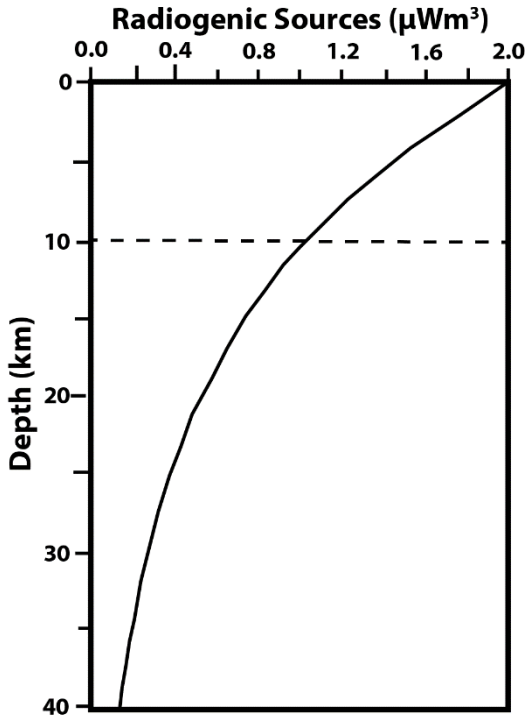

Figure 1. Distribution of radiogenic heat sources with depth in the Earth's continental crust.

Modified from Singh and Manglik (2000).

However, there are cases where residual, deep crustal granulites (including ultrahigh-temperature granulites, >900 °C) retain high radiogenic heat production. These regional-scale examples from southern and eastern India, South Africa, Brazil, and Finland demonstrate that the deep/lower crust is not necessarily always deficient in radiogenic heat production. Moreover, studies – including experimental – show that Th is less compatible than U in melt (Rudnick et al. 1985, Stepanov et al. 2012), with the important implication

that if monazite (the chief Th reservoir in rocks) can be retained in the residuum, granulite-facies crust maybe characterised by high radiogenic heat production. Such a view is in direct contrast with the standard view of geochemical differentiation of the crust. Therefore, the abundance and distribution of radiogenic heat production with depth in Earth is seemingly not well understood as the standard view provides. Given the natural examples of deep crust that have high radiogenic heat production, supported by Stepanov et al. (2012) and Rudnick et al. (1985), a set of scenarios should exist in which melting and melt loss leads to enrichment in HPE concentrations in the metamorphic residuum. These scenarios are logically more likely to occur in rocks such as metapelites and metapssamites that contain abundant fluid, monazite and bulk compositions that are conducive to abundant melt generation.

In this study, K–Th–U concentration data and phase equilibria modelling are used to monitor the changes in crustal heat production arising from progressive up-temperature metamorphism, including melt production and loss. The study is focussed on a single metasedimentary unit within the Reynolds Range, central Australia, that records metamorphism from subsolidus (greenschist) to suprasolidus (granulite) conditions, where preliminary data indicates that radiogenic heat production increases as a result of partial melting and melt loss. It is likely that a compositional threshold exists whereby melt loss leads to HPE enrichment in the residuum, principally via Th-hosting solid solution in monazite. Enrichment of heat production concentration in the residuum arising from melt loss has profound consequences for the tectonic stability of metamorphosed crust, the geochemical organisation of the crust, and its thermal potential (Sandiford et al. 2001).

Methods

GAMMA RAY SPECTROMETERS

For sampling outcrops in the field, Radiation Solutions' (RS) RS 230 BGO SuperSpec devices, which are handheld portable gamma ray spectrometers, were used to directly determine the K-U-Th contents at the outcrop. Three of the devices were used at each outcrop primarily to reduce the variation in element concentration that may occur within a single location. Data was acquired across 5 separate traverses spanning from greenschist to granulite grade (Figure 2).

The portable GRS devices work by detecting passing gamma rays with a large 2 by 2 inch bismuth germanium oxide (BGO) crystal detector and creating a spectrum by plotting the count of gamma rays over the sample period versus their energy. This spectrum plot is then analysed by systems within the device, measuring the number of gamma rays between specific energy levels indicative of the presence of decaying potassium, thorium and uranium and their more active isotopes. This count is then translated by the internal firmware and displayed on the screen on the front of the device as quantity percentages and parts per million of potassium, thorium and uranium.

Specially designed concrete pads at the Geoscience Australia facility in Therbarton, a suburb of Adelaide, were used to calibrate the GRS devices. Each of the pads has known quantities of KUTh and was used to calibrate the devices and scale them correctly before being taken into the field. This process was undertaken using the instructions provided by the manufacturer in the documentation accompanying the devices. The same slabs were also used to check the readings on the devices when they were returned from the field in order to calculate possible error due to drift over time.

Pre-use:

Prior to field work, the devices were calibrated to a known standard, which were the calibration pads at the DIMITRE yard at Thebarton in Adelaide.

Manuals and further technical information of the RS 230 devices can be found by contacting Radiation Solutions and on the information page found at:

http://www.radiationsolutions.ca/index.php?id=78

Taking samples:

When taking samples, the devices were turned on at each new location and allowed to stabilise to the background for at least 10 minutes prior to sampling. The devices were placed on outcrops with the flat front plates of the devices acting as their base, flush against the rock. The active detection area of the devices is around the first half cubic meter surrounding the head of the device, so as much of this area was filled with outcrop as possible. Outcrops that were chosen to be measured were typically of half a cubic metre in size or larger. Once in place, the assay process was initiated on each device and allowed to run for 180 seconds. This time was chosen due to Radiation Solutions' recommendation that the devices could return very accurate readings over this time, while also allowing many samples to be taken efficiently over a short period of time in the field. After the devices had completed their assays, their readings of the concentration of potassium, uranium and thorium were recorded. A GPS location for each traverse was taken for classification of the sample location metamorphic grade with regards to other literature on the field site.

The devices were turned off and returned to their cases for transportation between traverses. They were then restabilised at each new location.

The KUTh data was converted into heat production using the formula:

$$H_r = [U]\left(H_U + \frac{[Th]}{[U]}H_{Th} + \frac{[K]}{[U]}H_K\right)$$

$$\begin{aligned} \text{where} \quad H_U &= 9.71 \times 10^{-5} \quad \text{W/kg} \\ H_K &= 3.58 \times 10^{-9} \quad \text{W/kg} \\ \text{and} \quad H_{Th} &= 2.69 \times 10^{-5} \quad \text{W/kg} \end{aligned}$$

Equation 1. Heat production rate from KUTh concentration.

H_u is the heat release and [ ] is the concentration of the element. After Turcotte and Schubert (2002).

Results

OUTCROP DETERMINATION OF K-U-Th

Figure 18 shows the location of the traverses across the Pine Hill Formation used to evaluate the change in crustal heat production with increasing metamorphic grade.

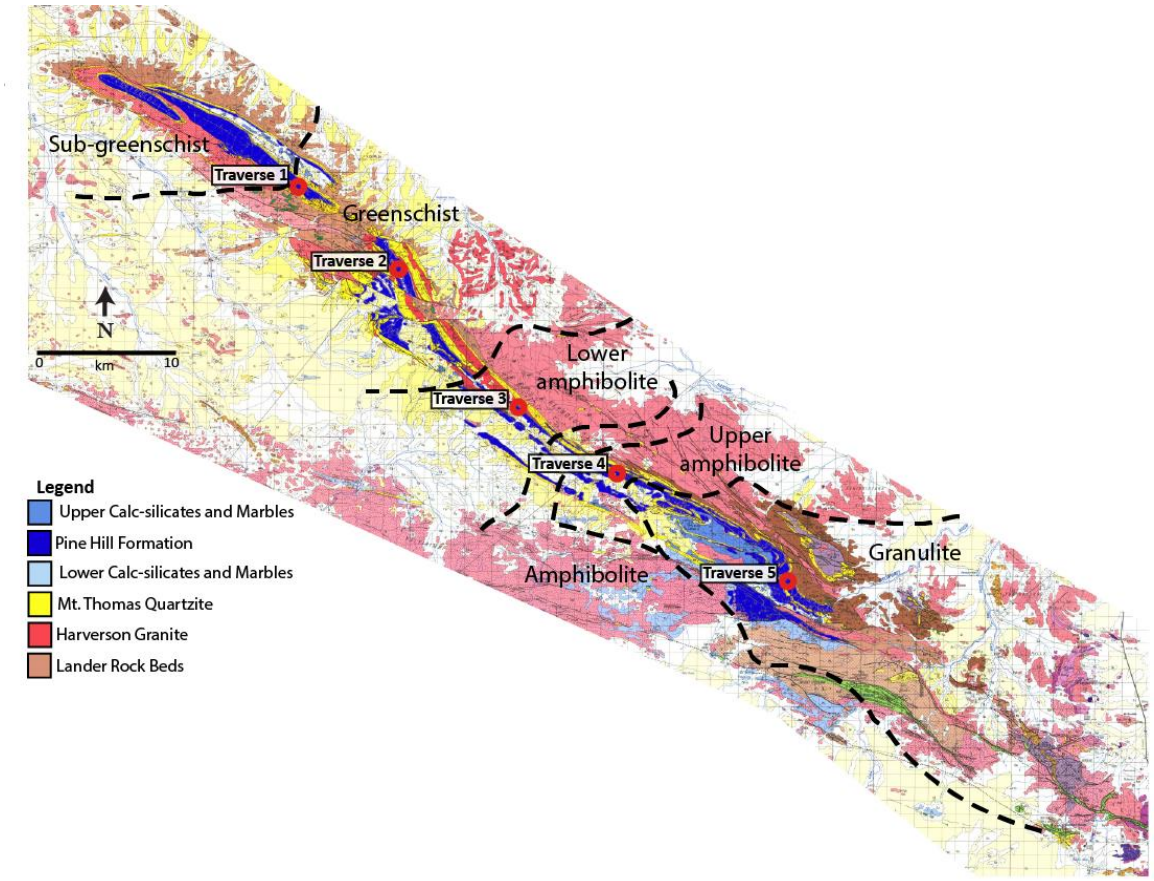

Figure 2. Detailed map of Reynolds Range showing the locations of the traverses used to study KUTh concentration.

Isograds form the 1600–1530 Ma Chewings event are shown. Modified from (Stewart et al. 1981).

GAMMA RAY SPECTROMETER DATA

Data collected from portable GRS devices of the concentrations of KUTh in each traverse is shown below.

Table 1. Traverse 1

K_2O (wt%)			**U (ppm)**			**Th (ppm)**		
4.33	4.26	1.89	3.93	2.93	3.36	14.40	7.89	3.48
1.59	1.82	5.01	3.55	4.01	3.66	6.54	22.04	20.80
4.83	5.08	4.49	4.10	4.43	4.05	16.91	14.20	14.68
4.50	4.78	5.86	4.54	4.33	3.98	16.70	21.03	17.64
6.00	5.72	6.12	4.05	3.76	3.20	19.88	19.10	23.11
5.89	5.88	4.93	3.75	3.15	2.83	19.52	18.66	21.03
4.71	4.59	5.34	3.22	1.94	2.98	18.15	15.61	19.12
5.10	5.10	5.23	1.97	3.14	3.63	19.39	17.55	17.63
5.19	5.14	6.20	2.87	3.55	2.95	19.45	21.18	19.00
6.08	5.85	6.60	4.19	3.20	3.31	19.11	19.15	19.82
6.51	6.43	5.91	2.91	3.03	2.84	21.15	18.15	18.27
6.00	5.97	5.63	3.47	2.72	4.14	22.18	15.50	17.39
5.74	5.72	5.91	3.09	3.16	2.94	20.13	16.90	20.23
5.62	5.95	5.99	3.99	3.34	4.74	15.81	20.37	15.71
5.88	5.92	5.71	2.64	3.85	2.95	18.05	18.18	15.83
6.05	5.85	6.22	3.63	3.70	3.10	19.61	17.62	19.16
6.09	6.27	5.90	4.03	2.59	3.92	19.55	21.37	19.68
6.02	6.09	6.86	3.49	3.69	3.46	16.87	22.93	20.46
6.74	6.65	4.85	4.67	3.24	2.71	22.25	16.19	17.79
4.91	4.96	5.34	3.23	3.23	3.30	14.73	15.59	19.60
5.06	5.19	5.19	2.70	3.34	5.22	18.86	17.52	19.79
5.30	5.34	6.16	3.42	4.46	4.07	19.12	20.36	23.73
6.23	6.35	6.47	4.82	2.88	2.99	23.87	21.92	18.79
6.15	6.43	5.95	3.24	3.97	3.56	19.71	20.47	16.48
6.00	6.13	6.12	3.49	3.42	3.12	18.49	19.21	17.79
5.90	5.73	5.50	3.39	2.89	3.21	16.34	19.11	20.35
5.63	5.65	5.79	3.26	3.53	3.83	17.61	19.30	19.20
5.87	5.85	5.34	3.86	3.57	4.21	20.80	17.94	21.15
5.17	5.19	5.56	4.07	4.03	4.29	20.53	21.16	22.96
5.62	5.72	5.97	4.52	3.60	3.79	22.81	20.82	19.18
5.96	5.99	6.36	4.16	3.66	4.09	17.79	19.90	19.12
6.24	6.23	6.01	4.16	3.01	4.34	19.62	21.02	19.04
6.13	5.93	6.23	2.84	4.13	3.81	18.81	21.61	21.92
6.09	5.94	6.25	3.70	4.36	3.03	24.37	22.94	23.81
6.40	6.43	6.53	4.60	4.03	3.46	22.07	19.62	23.99
6.78	6.59	5.64	3.44	3.35	3.63	19.21	17.46	19.77
5.78	5.93	4.57	3.05	2.85	3.29	20.25	14.54	15.80
4.71	4.81	6.04	3.39	3.44	4.34	17.19	15.91	18.18
5.74	6.00	4.86	4.02	3.92	2.25	20.88	14.83	15.15

K_2O (wt%)			**U (ppm)**			**Th (ppm)**		
4.95	4.65	4.81	3.32	2.75	3.50	12.43	19.64	16.18
4.79	5.01	5.16	2.94	4.32	4.61	17.82	18.96	16.37
4.97	5.34	5.29	3.76	4.08	3.53	19.11	19.86	19.65
5.06	5.11	4.62	4.56	4.02	4.71	21.15	13.46	16.23
4.44	4.73	7.10	4.52	4.69	3.52	17.76	26.32	23.37
7.22	6.95	3.75	5.29	3.30	4.93	27.61	13.58	14.65
3.58	3.50	5.85	3.62	3.93	4.96	12.60	19.66	20.16
5.88	5.89	6.19	5.05	4.08	4.44	23.40	18.27	22.84
6.08	6.03	6.82	4.93	4.06	3.59	20.01	19.91	24.44
6.80	6.74	6.62	4.08	4.01	4.67	20.92	21.21	18.98
6.68	6.55	6.22	3.78	4.77	3.68	20.36	19.17	22.71
6.48	6.57	5.62	5.03	4.23	2.92	20.61	19.36	18.92
4.49			3.81			15.45		

Table 2. Traverse 2

K_2O (wt%)			**U (ppm)**			**Th (ppm)**		
3.4	2.2	6.4	4.1	4.7	4.5	17.1	17.9	23.7
3.6	3.6	3	3.8	4.6	4	14	14.1	23.6
3.2	4.1	3.5	4.5	3.6	3.7	15.4	17.5	28.2
3.5	7.1	2.9	3.3	3.1	3.5	14.3	16.7	22.4
3.9	4.8	2.7	3.5	3	5.2	16.9	17.3	21.5
3.8	7	2.5	3.4	4.7	4.8	17.3	17.3	19.3
4.1	4.9	2.3	5.2	4	4.1	14.5	14.8	20.4
2.8	4	4.4	4.5	6.8	5	16.5	20.6	19.8
3.9	3.8	3.6	4.2	7.8	4.3	18.6	20.7	19.5
2.9	4.1	6	5.3	4.7	5.2	16.3	17.3	22.7
2.9	3.8	5	4.9	4.6	4.9	18.5	15.7	22.3
3.7	5.7	4.7	4.7	6	5.4	14.9	18.3	23.9
3.4	7.3	4.4	3.8	4.1	3.9	17	23.6	21.3
2.1	7	4.2	3.5	3.6	4.4	16.1	17.3	23.9
5.4	7.2	5.3	5.5	4.8	3.5	20.1	23.6	20.9
4.2	4.1	5.2	5.2	4.1	4.1	19.2	17.2	21.8
2.4	3.3	4	2.8	4.4	3.1	13.7	20.2	25.1
1.2	4	3.4	3.5	3.4	5.6	14.3	16.8	23.8
3	3.5	3	2.6	3.6	5.7	14.3	16.6	24
4.7	4.4	4	6.2	4.5	4.4	25.1	19.1	24.9
4.7	4.9	2.9	4.3	4.4	5.9	20.9	21.5	22.7
4.7	3.6	4.4	5.7	6.4	5.4	22.6	27.2	18.7
5.5	3.8	4.4	4.9	6.3	4.3	24.5	25.8	21.6
3.1	3.4	3.6	4.2	7.7	4.5	18.5	28.2	15.7
3.5	6.7	2	4	5.2	4.3	19.3	21.8	16.1
3.2	6.1	3.5	4.4	4.5	6.5	18.6	20.2	15.9
3.3	5.2	5	5.1	4.9	3.8	23.3	21	17.8
3.6	5.1	5.6	6.4	7.1	7	20.5	18.8	18.2
3.1	5.2	5.1	6	7.7	5.4	18.8	22.3	15.1
3.5	5	3.5	4.2	5.9	6.5	17.1	20.3	19.8
2.2	5.5	3.2	3.6	6.6	5.1	12.2	20.7	18.2
5.3	5.2	4.1	4.9	4.3	4.1	23.5	18.3	18
5.6	5.5	3.7	4.8	4.9	4.2	23.7	20.2	17.4
4.1	3.6	4.5	6	6.2	6.6	19.6	25.1	19.4
4.9	4.7	2.9	6.6	6.9	5.6	19.2	23.2	23.6
4.2	3.2	5	6.6	5.6	5.4	19.7	22.1	19.7
4.1	2.7	4.1	5.4	5.3	5.5	20.9	21.4	20.1
4.9	3.4	3.6	5.3	5.5	5	21.2	22.7	17.5
3.9	4	3.4	6	5.9	6.7	20.1	20.5	14.4
3.5	4.3	3.3	4.9	6.6	5	19	25.5	20.6
3.8	2.5	3.9	4.5	7.1	4.1	15.1	24.7	24.7
4.5			5.2			16.9		

Table 3. Traverse 3

K_2O (wt%)		**U (ppm)**		**Th (ppm)**	
5.9	3.2	5.4	3.9	26.8	20.2
4.2	3.6	3.6	4.8	23.1	19.2
5.1	3.7	5.1	3.8	20.3	20
5.8	4.2	5.4	6.3	25.1	21.1
3.4	6	4.7	5.6	20.2	27.4
3.5	4.5	4.7	4.8	22.2	20.3
4.6	4.2	5	3.9	23.9	21.2
4.8	5.3	4.5	4.4	25.3	24.8
5.3	4.3	5.2	4.9	23	23.9
3.6	4.1	4.9	3.5	17.2	24.3
4.3	4.3	5.2	4.8	19.9	23.3
5.2	4.3	4.5	4	26.9	22.1
4.3	2.9	4.9	3.9	23.9	18.7
4	4.3	4.8	4.7	17.6	24.8
4	3.1	5	3.5	23.7	15.7
4.7	3.7	5.1	2.9	23.6	20.5
4.4	3.6	4.6	4.4	22.6	18.5
4.6	5.3	4.8	4.2	21	23.4
5	5.2	4.3	4.3	19.5	22.4
3.6	4.6	4	5.1	20.3	19.9
4	4.3	4.9	4.2	21.9	21.4
3.3	4.4	5.3	4.2	19.3	23.4
4.3	4.6	3.7	4.9	22.8	19.2
4.8	5.1	4.9	5.6	25.4	20.9
4.4	4.4	5.3	4.5	23	19.3
5.1	4.9	4.9	5.7	25.3	20.7
5.1	5.5	4.8	5.8	23.5	24.7
4.5	5	5.1	4.9	18.7	23.8

Table 4. Traverse 4

K_2O (wt%)		**U (ppm)**		**Th (ppm)**	
5.3	6.6	8	5.8	31.4	26.9
6.9	4.7	8.7	5.4	33	23.6
6.7	4.7	9.2	5.4	33.4	26.6
4.5	5.1	7.1	7.2	28.8	22.7
5.3	5.7	8.5	5.5	33.5	26.5
5.5	4.3	8.4	6.1	32.8	24
5.8	5.6	11.4	5.9	31.8	23.3
6.5	5.8	8.9	5.6	35	24.8
5.2	4.6	7.3	5.4	28.4	22.1
4.9	4.7	8.3	6.6	23.9	24.8
5.4	4	7.4	6.7	29.1	22.7
4.8	5.5	7.1	8.4	23.4	31.4
4.4	6	5.2	9.3	24	32
4.9	7	5	14.3	24.4	42.2
4.5	6.8	5.9	11.8	24.2	36.2
5	5	6	10.6	23.1	30.4
4.7	3.8	5.3	8.9	25.2	25.7
4.4	5.8	5.3	10.3	25.4	31.9
3.9	5.7	6	9.1	25.3	34.4
5.1	5.7	4.7	7.8	27.5	31.4
5.4	3.7	5.1	5.5	25.5	24
4.8	5	5.4	5.3	24.1	24.5
4.5	5.4	5.6	5	20.9	27.5
6.5	5.1	8.2	6.1	27.5	28.3
5.1	6.6	9.3	6.6	23.5	24.2
6.9	4.8	12.3	7	32.6	26.5
5.8	5.8	10.7	5.7	36.6	30.1
6	3.9	16.5	4.1	32.6	25.4
6.7	5	14.8	5.7	32.5	29.2
5.1	5	10.2	5.5	28.3	26.4
6.5	4.5	14.3	4.7	30.7	22.7
5.8	5.2	10.6	6.4	30.5	26.8
4.3	6.3	6.5	5.5	35.9	23.8
8.1		7.3		31.8	

Table 5. Traverse 5

K_2O (wt%)			**U (ppm)**			**Th (ppm)**		
5	5.15	5.51	2.83	2.64	3.08	31.22	28.07	28.54
5.32	4.62	3.47	2.45	1.81	3.1	28.27	25.34	30.27
6.97	3.62	5	3.37	2.26	3	34.86	21.37	35.6
3.17	4.21	5.03	2.18	2.44	2.26	18.61	21.44	23.28
4.86	5.74	7.51	2.87	2.42	2.41	28.47	31.18	29.48
5.38	5.44	5.14	3.81	2.73	2.96	27.95	24.55	27.22
4.15	5.13	5.63	2.89	2.47	3.37	22.77	27.62	25.7
5.11	4.94	5.55	2.43	2.97	3.19	29.17	30.21	29.96
3.46	4.9	5.66	1.48	2.12	2.29	22.83	25.46	21.68
6.44	5.04	4.39	2.68	2.63	2.24	29.66	24.38	30.16
5.28	4.65	4.31	2.73	2.35	3.17	29.8	21.88	29.33
6.71	6.98	5.06	2.06	3.15	2.3	37.4	29.26	34.69
6	7.13	4.88	2.52	2.49	2.46	27.77	32.43	26.63
5.16	5.51	4.33	3.4	2.82	3.58	39.74	25.52	38.48
6.87	3.59	3.71	3	3.01	3.16	31.67	26.3	29.72
6.87	4.76	5.15	3.45	3.72	3.49	30.46	26.97	30.95
5.08	4.91	5.13	3.32	4.07	2.75	32.79	28.54	32.89
4.1	5.1	5.87	2.52	3	4.34	24.43	23.32	43.66
4.71	5.2	4.09	2.52	2.7	3.19	25.89	29.69	29.83
4.34	4.15	7.05	2.11	2.99	2.94	24.7	27.99	26.08
2.52	3.68	7.62	2.47	3.21	3.25	25.48	27.7	32.64
4.89	4.87	5.81	2.58	3.51	3.31	31.46	30.39	25.75
4.4	4.31	3.85	3.16	4.88	2.2	23.14	39.9	24.17
4.1	4.27	5.28	2.63	3.27	1.89	28.46	33.64	28.98
4.22	5.7	5.2	3.44	3.03	1.72	25.45	29.19	22.71
4.44	4.33	4.18	2.35	3.84	2.45	27.61	29.15	21.23
5.18	4.43	6.58	2.36	2.89	2.11	26.7	24.52	25.53
4.14	5.13	4.87	2.37	2.52	2.67	22.51	32.09	28.13
6.78	5.82	4.09	3.21	3.11	2.26	30.24	32.77	28.87
6.02	5.55	5.05	2.14	3.42	3.41	33.19	35.64	26.55
5.91	3.01	4.66	2.61	2.05	2.19	26.83	17.94	23.82
3.3	4.13	3.56	2.46	2.61	3.02	22.68	28.24	27.39
4.5	4.59	4.3	3.32	3.05	2.41	30.64	32.92	22.27
5.38	5.06	5.53	3.83	2.77	2.91	28.92	24.63	30.18
5.85	4.56	5.37	2.82	2.56	2.85	27.65	32.92	30.57
6.58	4.67	5.1	2.83	2.23	2.63	31.47	23	29.46
4.92	6.53	5.98	2.94	1.82	2.71	28.42	29.78	21.72
3.65	5.79	5.86	3.25	2.76	3.7	27.7	32.55	28.65
4.61	7.45	3.95	3.35	2.8	4.16	28.62	37.11	28.92
5.32	5.65	5.24	4.64	3.23	2.61	45.28	27.85	28.54
5.04	5.07	5.58	2.67	3.48	3.01	33.22	35.41	27.57
5.91	4.93	4.24	3.08	2.6	2.75	24.37	31.67	26.6
4.72	5.86	3.69	4.04	2.82	2.76	29.03	29.96	30.34
3.16	4.85	4.69	3.58	2.46	3.47	23.29	28.68	32.88

K–U–TH DISTRIBUTION AND HEAT PRODUCTION

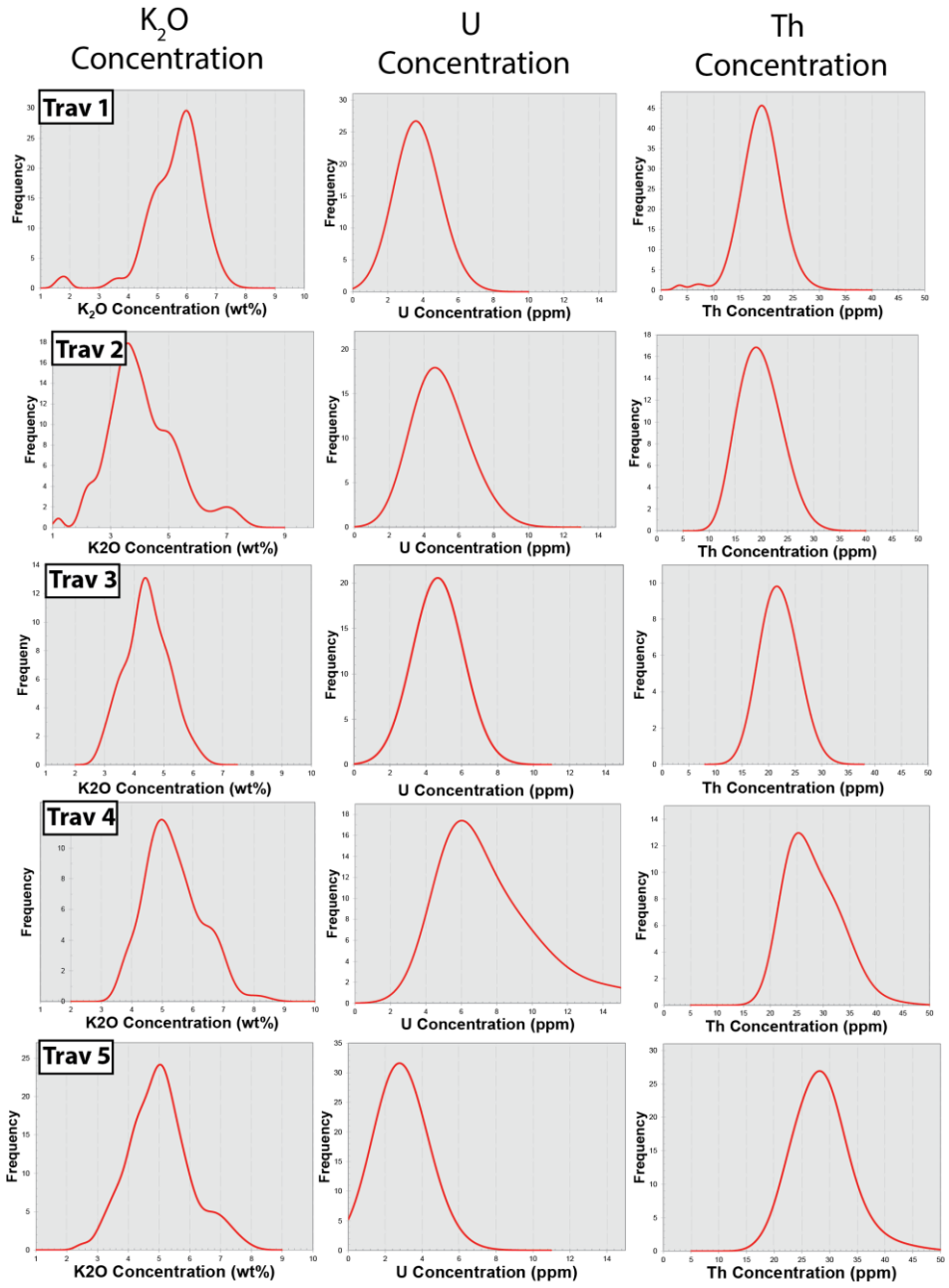

Figure 3. Concentration of potassium, uranium and thorium with increasing metamorphic grade.

Weighted averages for KUTh in each traverse used in this study.

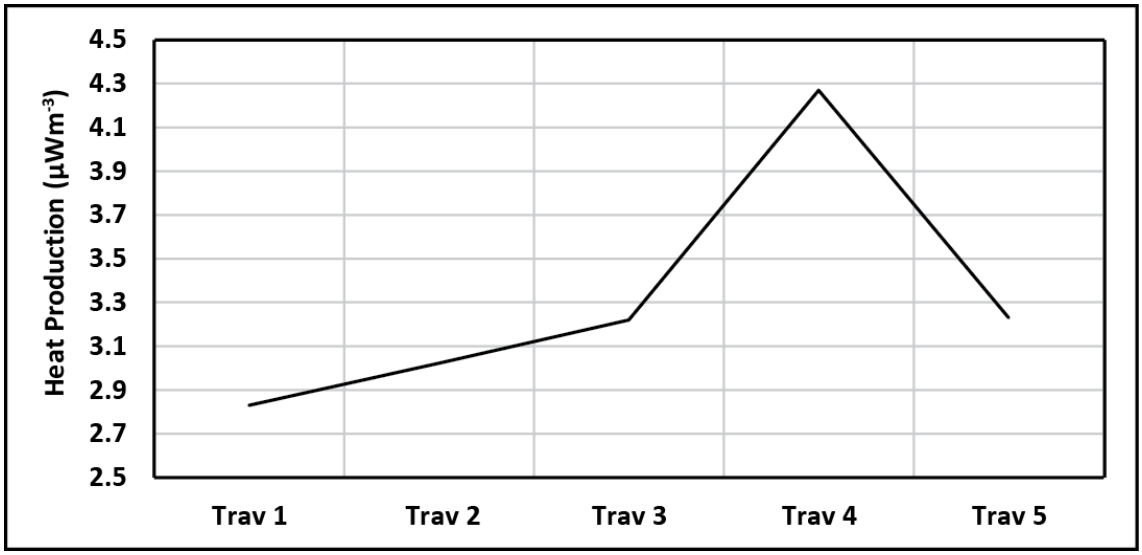

Figure 4. Heat production with increasing metamorphic grade in Reynolds Range.

REPRESENTATIVE MONAZITE MICROPROBE ANALYSES

Monazite grains were analysed from lower amphibolite to granulite facies in order to assess the changes in the concentration of KUTh.

Table 6. Average monazite microprobe analyses use to assess the U and Th distribution. A total of 50 analyses were done for Traverse 2 (lower amphibolite), 141 for Tarverse 3 (amphibolite), 59 for Traverse 4 (upper amphibolite) and 88 for Traverse 5 (granulite).

	Traverse 2		**Traverse 3**		**Traverse 4**		**Traverse 5**	
	RR2015 3-20	RR2015 3-25	RR2015 1-20	RR2015 1-1	RR2015 2-8	RR2015 2-16	RR2014 -8	RR2014 -9
Si WT%	0.24	0.23	0.23	0.21	0.18	0.35	0.32	0.43
Pb WT%	0.34	0.33	0.40	0.34	0.35	0.32	0.41	0.36
Th WT%	4.07	4.14	4.44	3.80	4.27	4.03	5.10	4.85
U WT%	0.23	0.24	0.40	0.33	0.25	0.18	0.29	0.15
Y WT%	1.20	1.24	1.69	1.85	1.91	2.30	2.30	2.25
La WT%	11.69	11.88	11.35	11.55	11.25	10.73	11.32	11.35
Ce WT%	24.02	23.84	23.55	24.55	24.76	22.98	24.34	23.76
Pr WT%	2.44	2.41	2.37	2.42	2.40	2.40	2.30	2.37
Nd WT%	9.07	8.94	8.78	9.10	8.79	9.03	8.51	8.82
Sm WT%	1.51	1.39	1.48	1.52	1.41	1.48	1.33	1.38
Gd WT%	1.20	1.05	1.28	1.24	1.24	1.30	1.19	1.21
Ca WT%	0.68	0.67	0.80	0.69	0.76	0.73	0.70	0.53
P WT%	13.74	13.90	13.57	13.43	13.05	13.79	13.26	13.05
O WT%	27.72	27.87	27.54	27.51	27.00	27.87	27.48	27.18
TOTAL	**98.15**	**98.14**	**97.87**	**98.54**	**97.61**	**97.50**	**98.85**	**97.69**
SiO2	0.51	0.50	0.51	0.45	0.39	0.75	0.68	0.88
PbO	0.36	0.35	0.44	0.36	0.37	0.34	0.44	0.41
ThO2	4.63	4.71	5.10	4.33	4.86	4.59	5.81	5.78
UO2	0.26	0.27	0.49	0.38	0.28	0.21	0.33	0.20
Y2O3	1.53	1.58	2.21	2.35	2.42	2.92	2.92	2.75
La2O3	13.71	13.94	13.32	13.54	13.19	12.58	13.28	13.31
Ce2O3	28.13	27.92	28.19	28.75	29.01	26.91	28.51	28.40
Pr2O3	2.85	2.82	2.76	2.83	2.81	2.81	2.69	2.74
Nd2O3	10.58	10.43	10.08	10.61	10.25	10.53	9.92	10.16
Sm2O3	1.75	1.62	1.70	1.77	1.64	1.72	1.55	1.59
Gd2O3	1.39	1.21	1.48	1.43	1.43	1.50	1.37	1.39
CaO	0.95	0.93	1.17	0.96	1.06	1.02	0.98	0.80
P2O5	31.49	31.86	30.63	30.77	29.91	31.61	30.37	29.08
O	0.00	0.00	0.00	0.00	0.00	0.00	0.00	0.00
TOTAL	**98.15**	**98.14**	**98.11**	**98.54**	**97.61**	**97.50**	**98.85**	**97.50**

Discussion

KUTH DISTRIBUTION WITH PROGRESSIVE METAMORPHISM

Figure 3 shows that, while it varies from traverse to traverse, there is no real change in the concentration of K_2O with increasing metamorphic grade. The K_2O concentrations determined by GRS are higher than the corresponding concentrations determined by XRF by around 1-2wt% (shown in Appendix 2). The reasons for this are not clear. The GRS units were calibrated before use and returned the correct K_2O value for the calibration pad at Thebarton. One possibility for the discrepancy is that the GRS units have a much larger sample volume than a geochemical hand sample, and may inadvertently oversample K_2O derived from accumulations of detrital biotite that accumulate in the soil at the outcrop. Nonetheless, the relative change in K_2O derived from the GRS units is valid.

The GRS data show that with increasing grade, the concentration of U decreases. This is consistent with U loss in fluid as prograde metamorphism dehydrates the rock mass, and as melt is lost from the higher grade regions. The exception is Traverse 4, in which the concentration of U is significantly elevated. This may be an analytical artefact. The region around traverse 4 has very limited outcrop and the traverse was done in a deep gully to access the available outcrop. Areas surrounded by close topography are not ideal for GRS U analyses due to over sampling created by detection of incident gamma rays generated in the adjacent topography.

In contrast to U, Th concentrations increase. The primary reservoir for Th in metapelitic rocks is monazite (Bea 1996, Bea and Montero 1999). Based on what is understood

about the solubility of monazite in granitic melts (e.g. Kelsey et al. 2008), it would be logical to expect that monazite abundance would decrease in regions that had undergone melt loss. Models from this study for melting and melt loss in the Pine Hill Formation suggest that around 20% melt loss occurred from the granulitic parts of the Pine Hill Formation, thus while it is inevitable that monazite dissolution and loss occurred during melt loss, the Th content of the rocks did not decrease. Table 6 shows the average compositions of monazite in rocks that range from amphibolite to granulite grade. It is clear that the Th content of the monazite increases with increasing metamorphic grade. This increase in Th content is also matched by an increase in Si content. These increases are consistent with progress of the monazite ($CeLaPO_4$) - huttonite ($ThSiO_4$) solid solution (Foerster and Harlov 1999). Progress of this solid solution serves to buffer the Th content of the rock system as monazite dissolution occurs by concentrating Th into the residual monazite.

Implications for metamorphic induced differentiation of crustal heat production

There are some limitations with the modelling approach that has been used to explore melt loss and the validity of melt reintegration in the Pine Hill Formation. However, the results, in combination with geochemical data, have potentially important implications for metamorphically induced crustal differentiation, particularly differentiation of the heat producing elements K, U and Th (KUTh).

Most models for the crustal distribution of KUTh show a highly depleted lower crust, coincident with granulite grade rocks, and an upper crust significantly enriched in KUTh (e.g. Oxburgh 1980, Singh and Manglik 2000). This distribution is commonly

considered to be strongly induced by metamorphic processes that involve partial melting and melt loss, with the removal of KUTh from regions that have granulite facies metamorphism (Bea 1996, Bea and Montero 1999, Arevalo Jr et al. 2009). One consequence of this removal of KUTh is that melting and melt loss from granulite domains should result in long term lithospheric cooling and strengthening (e.g. Sandiford et al. 2002), thereby strongly influencing the way the crust responds to subsequent tectonic events (Sandiford et al. 2002). However despite the broad acceptance of these models there have been essentially no studies that examine the way in which KUTh change within a single rock unit that spans the transition from subsolidus to suprasolidus conditions.

The results of this study show that for the Pine Hill Formation metapelite, increasing metamorphic grade, melting and melt loss did not deplete the volumetric heat generation rate as is commonly assumed to occur as a consequence of granulite facies metamorphism (Oxburgh 1980, Singh and Manglik 2000). While loss of KUTh must have occurred during melt loss, this loss was offset by volume loss, such that the concentration of HPE's in the residual granulite is not significantly different to their concentration in the protolith. It is increasingly being recognised that many high grade metasedimentary terrains have much higher heat production rates than allowed for in typically applied models for the geochemical structure of the crust (e.g. Andreoli et al. 2006). It is likely that the conventional models for the way in which heat production is commonly distributed in the crust, are more a reflection of the lithological assembly of crustal columns and not of chemical differentiation associated with high grade

metamorphism. If this is the case, then high-grade terrains have the potential to exert significant thermal affects during later reworking.

APPENDIX 2: WHOLE-ROCK GEOCHEMISTRY

Traverse1

	RR2014-1A	RR2014-1B	RR2014-1C	RR2014-2A	RR2014-2b	RR2014-2c	RR2014-2d	RR2-14-3a1	RR2014-3a2
Major elements (wt%)									
SiO2	70.40	70.55	70.76	66.62	61.34	68.55	66.60	77.64	77.93
TiO2	0.55	0.54	0.55	0.55	0.63	0.48	0.53	0.22	0.21
Al2O3	15.21	15.14	15.48	15.83	19.68	13.41	15.33	6.79	6.49
Fe2O3T	4.22	4.15	4.12	7.16	6.55	7.55	6.90	9.04	9.41
MnO	0.03	0.03	0.03	0.04	0.03	0.04	0.03	0.05	0.05
MgO	1.43	1.42	1.41	2.37	2.13	2.39	2.20	1.97	2.08
CaO	0.05	0.05	0.05	0.08	0.07	0.09	0.08	0.04	0.04
Na2O	0.09	0.08	0.08	0.10	0.13	0.07	0.09	0.00	0.01
K2O	5.22	5.19	5.13	4.57	6.10	3.59	4.44	1.27	1.05
P2O5	0.07	0.07	0.07	0.11	0.11	0.12	0.11	0.11	0.11
Total	**99.84**	**99.76**	**100.25**	**100.19**	**99.85**	**99.88**	**99.93**	**100.09**	**100.35**
LOI	2.57	2.54	2.57	2.76	3.08	3.59	3.62	2.96	2.97
Trace elements (ppm)									
Rb	372.8	364.8	369.4	250.9	346.0	181.3	247.1	70.6	58.7
Sr	28	30	30	20	27	18	21	10	8
Y	36.1	32.7	32.1	28.6	31.5	31.0	30.8	24.0	26.8
Zr	290	284	282	173	176	185	193	135	131
V	65	66	67	72	87	61	79	35	40
Ni	32	32	32	37	34	39	36	19	18
Cr	52	50	55	68	78	54	56	36	44
Nb	16.2	16.8	15.2	14.7	17.6	11.8	14.1	4.6	4.7
Ga	23.8	23.3	22.8	23.4	28.6	20.0	23.4	11.9	11.3
Cu	8	8	7	7	7	8	7	109	106
Zn	32	32	31	62	48	66	58	73	77
Co	7	7	7	24	19	25	22	26	27
Ba	1360	1311	1347	523	807	431	582	196	157
La	56	56	56	45	48	41	43	26	24
Ce	128	117	120	100	120	93	101	53	51
U	1.3	0.7	0.9	1.9	0.8	<0.5	0.5	<0.5	<0.5
Th	32.0	30.0	31.0	31.0	31.0	34.0	36.0	26.0	27.0
Sc	10	10	10	12	14	10	11	5	6
Pb	4	2	2	3	<1	<1	<1	5	<1

LOI, loss on ignition; Fe2O3T, total FeO and Fe_2O_3

	RR2014-3b	RR2014-3c	RR2014-4a	RR2014-4b	RR2014-4c	RR2014-4d	RR2014-5a	RR2014-5b	RR2014-5c	RR2014-5d
Major elements (wt%)										
SiO2	77.42	78.47	66.65	66.40	65.92	65.88	66.06	66.26	66.05	66.85
TiO2	0.21	0.21	0.56	0.57	0.56	0.59	0.58	0.56	0.56	0.56
Al2O3	6.66	6.82	16.40	16.25	16.54	16.53	17.64	17.72	17.51	17.26
Fe2O3T	9.17	8.84	6.13	6.00	6.23	5.98	5.07	4.94	4.95	5.01
MnO	0.05	0.05	0.04	0.04	0.05	0.04	0.02	0.02	0.02	0.02
MgO	2.06	1.95	1.67	1.64	1.67	1.69	1.42	1.45	1.48	1.45
CaO	0.04	0.04	0.10	0.09	0.10	0.08	0.02	0.03	0.03	0.03
Na2O	0.01	0.01	0.12	0.11	0.12	0.12	0.14	0.13	0.14	0.14
K2O	1.12	1.24	5.92	5.87	5.98	5.95	5.95	6.00	5.87	5.87
P2O5	0.11	0.12	0.09	0.09	0.10	0.09	0.08	0.07	0.07	0.07
Total	**100.78**	**100.59**	**100.51**	**99.93**	**100.14**	**99.80**	**100.00**	**100.24**	**99.75**	**100.34**
LOI	3.93	2.84	2.83	2.87	2.87	2.85	3.02	3.06	3.07	3.08
Trace elements (ppm)										
Rb	62.0	66.6	366.7	370.6	369.5	376.6	358.0	361.8	352.2	353.3
Sr	9	11	28	26	30	26	33	35	33	33
Y	25.5	24.3	15.5	15.3	15.9	15.0	17.5	18.4	16.5	17.7
Zr	134	127	211	192	208	184	193	191	188	189
V	36	37	76	72	76	72	81	78	76	75
Ni	19	18	47	46	48	45	31	34	32	33
Cr	42	60	64	70	69	73	72	65	79	68
Nb	3.8	4.5	14.2	14.4	13.9	14.2	15.0	15.1	15.7	14.4
Ga	11.8	11.7	23.5	23.8	24.2	24.1	26.9	26.8	25.6	26.0
Cu	107	99	17	17	15	17	21	24	25	25
Zn	75	70	67	67	68	68	43	47	47	47
Co	24	22	15	16	20	18	11	12	11	13
Ba	161	247	668	644	696	643	675	709	732	708
La	26	26	37	36	38	35	46	42	42	43
Ce	52	52	77	69	103	47	93	89	98	93
U	<0.5	<0.5	<0.5	<0.5	<0.5	<0.5	0.6	0.5	1.0	<0.5
Th	22.0	25.0	26.0	26.0	25.0	26.0	27.6	33.0	27.5	28.4
Sc	7	5	9	11	11	11	11	11	11	10
Pb	<1	<1	<1	<1	3	4	5	<1	<1	<1

LOI, loss on ignition; Fe2O3T, total FeO and Fe_2O_3

Traverse 2

	RR2015 1-2	RR201 1-3	RR201 1-6	RR201 1-7	RR201 1-8	RR2015 1-9	RR201 1-10	RR201 1-13
Major elements (wt%)								
SiO2	65.97	59.28	69.84	64.54	63.62	69.34	66.36	65.98
TiO2	0.69	0.67	0.72	0.62	0.57	0.71	0.63	0.55
Al2O3	18.77	22.12	16.70	19.96	22.97	17.42	19.62	20.20
Fe2O3T	7.44	7.90	6.17	6.92	5.86	6.91	5.19	5.26
MnO	0.15	0.05	0.07	0.08	0.07	0.09	0.05	0.04
MgO	1.73	2.58	1.53	2.00	1.41	1.74	1.14	1.51
CaO	0.16	0.12	0.06	0.11	0.07	0.11	0.06	0.06
Na2O	0.14	0.21	0.14	0.16	0.17	0.11	0.24	0.20
K2O	4.31	6.41	4.31	5.38	5.02	3.30	6.36	5.76
P2O5	0.05	0.07	0.05	0.07	0.07	0.07	0.08	0.07
Total	**99.41**	**99.41**	**99.59**	**99.84**	**99.83**	**99.80**	**99.73**	**99.63**
LOI	4.52	5.43	4.05	4.85	5.82	4.80	4.42	4.82
Trace elements (ppm)								
Rb	429	424	342	438	423	358	448	461
Sr	31	38	28	43	27	16	37	32
Y	29	14	25	21	56	28	23	28
Zr	144	111	200	140	151	161	156	116
V	87	99	91	87	77	92	79	76
Ni	66	61	62	51	65	71	61	58
Cr	123	115	144	117	113	155	119	117
Nb	22	15	19	15	13	20	15	16
Ga	30	29	25	28	34	28	28	31
Cu	18	22	18	26	22	43	19	15
Zn	58	38	39	72	36	62	34	31
Co	25	34	19	26	19	27	15	17
Ba	319	386	355	384	372	227	504	401
La	29	35	27	34	46	25	36	34
Ce	73	66	63	63	98	55	73	75
U	1	<0.5	<0.5	<0.5	2	<0.5	<0.5	<0.5
Th	29	31	28	26	47	33	27	29
Sc	15	15	13	12	12	15	12	11
Pb	<1	<1	<1	<1	1	<1	<1	1

LOI, loss on ignition; Fe2O3T, total FeO and Fe_2O_3

	RR201 1-14	RR201 1-19	RR201 1-20	RR201 1-21	RR201 1-24	RR201 1-25
Major elements (wt%)						
SiO2	66.90	61.11	65.25	62.28	62.74	64.20
TiO2	0.54	0.61	0.70	0.56	0.96	0.99
Al2O3	19.57	20.86	18.76	22.30	17.46	16.93
Fe2O3T	4.49	7.21	7.32	5.98	11.22	9.64
MnO	0.04	0.04	0.07	0.03	0.05	0.05
MgO	1.32	2.27	1.77	2.06	3.23	2.73
CaO	0.05	0.05	0.05	0.04	0.13	0.26
Na2O	0.25	0.23	0.22	0.22	0.64	0.85
K2O	6.81	7.41	5.98	6.11	3.19	3.89
P2O5	0.08	0.08	0.07	0.09	0.07	0.06
Total	**100.05**	**99.87**	**100.19**	**99.67**	**99.69**	**99.60**
LOI	3.15	4.44	3.99	5.48	1.30	0.88
Trace elements (ppm)						
Rb	448	419	408	371	156	184
Sr	40	47	31	64	37	56
Y	20	17	18	18	34	17
Zr	141	114	173	102	162	192
V	76	81	91	87	128	120
Ni	55	56	63	61	66	55
Cr	95	105	122	107	116	109
Nb	15	15	16	13	13	16
Ga	27	27	25	30	26	26
Cu	13	17	18	24	28	23
Zn	31	39	41	30	86	74
Co	12	25	22	20	43	32
Ba	453	411	467	420	413	418
La	33	35	35	38	37	34
Ce	60	70	68	68	78	72
U	2	<0.5	<0.5	<0.5	<0.5	1
Th	29	30	34	30	33	31
Sc	12	13	13	13	16	13
Pb	<1	<1	<1	<1	5	5

LOI, loss on ignition; Fe2O3T, total FeO and Fe_2O_3

Traverse 3

	RR2014-6D	RR2014-9D	RR2014-9E	RR2014-9F	RR2014-6a
Major elements (wt%)					
SiO2	65.39	68.97	70.28	69.45	65.64
TiO2	0.69	0.78	0.76	0.76	0.70
Al2O3	19.66	16.58	16.79	17.47	18.19
Fe2O3T	5.87	5.43	5.23	5.30	**5.39**
MnO	0.02	0.02	0.02	0.02	0.02
MgO	4.31	4.07	3.72	3.92	3.84
CaO	0.07	0.38	0.03	0.04	0.04
Na2O	0.10	0.13	0.08	0.08	0.05
K2O	4.08	3.17	2.88	3.04	4.35
P2O5	0.07	0.05	0.04	0.04	0.08
Total	**100.26**	**99.58**	**99.83**	**100.12**	**104.29**
LOI	1.73	1.27	1.15	0.25	1.79
Trace elements (ppm)					
Rb	189	167	156	169	204
Sr	29	16	14	14	28
Y	29	10	11	7	33
Zr	235	300	294	286	236
V	96	91	89	90	94
Ni	49	50	50	52	46
Cr	93	85	89	98	64
Nb	16	16	16	16	15
Ga	30	28	29	30	28
Cu	8	9	10	9	8
Zn	26	23	22	23	20
Co	21	17	16	14	20
Ba	696	592	500	541	714
La	33	27	29	27	36
Ce	80	63	63	53	88
U	<0.5	<0.5	1	1	<0.5
Th	40	36	39	35	37
Sc	12	10	8	9	13
Pb	<1	1	<1	<1	<1

LOI, loss on ignition; Fe2O3T, total FeO and Fe_2O_3

	RR2014-6b	RR2014-6c	RR2014-9a	RR2014-9b	RR2014-9c	RR2014-12a
Major elements (wt%)						
SiO2	63.72	63.97	66.07	66.13	68.58	62.53
TiO2	0.64	0.72	0.88	0.91	0.86	0.71
Al2O3	19.51	19.43	18.51	18.63	16.68	21.5
Fe2O3T	**5.84**	**6.18**	**5.95**	**6.1**	**5.62**	**5.55**
MnO	0.03	0.02	0.06	0.03	0.03	0.04
MgO	4.45	4.53	4.38	4.54	4.02	1.61
CaO	0.04	0.04	0.08	0.05	0.04	0.18
Na2O	0.04	0.03	0.03	0.02	0.02	0.36
K2O	3.82	3.16	2.83	2.58	2.86	6.31
P2O5	0.06	0.06	0.04	0.03	0.04	0.12
Total	**104.51**	**99.68**	**99.78**	**99.93**	**99.67**	**99.8**
LOI	1.86	2.05	1.34	1.31	1.29	1.36
Trace elements (ppm)						
Rb	186	168	162	148	157	335
Sr	24	23	27	16	18	37
Y	30	25	3	3	3	10
Zr	219	236	325	329	306	175
V	87	95	108	109	95	122
Ni	45	47	48	47	46	60
Cr	64	70	102	88	81	91
Nb	14	17	18	18	17	14
Ga	30	31	32	33	29	35
Cu	7	8	8	9	7	69
Zn	22	24	19	19	18	29
Co	23	25	21	23	18	12
Ba	660	544	647	559	592	690
La	36	32	20	16	19	31
Ce	84	72	34	31	39	65
U	1	1	<0.5	<0.5	<0.5	<0.5
Th	37	36	15	24	23	24
Sc	12	12	13	12	12	8
Pb	<1	2	<1	<1	<1	24

LOI, loss on ignition; Fe2O3T, total FeO and Fe_2O_3

APPENDIX 3: REPRESENTATIVE ELECTRON MICROPROBE ANALYSES

Sample 2014-9

	Ilmenite						Magnetite					
Si WT%	0.02	0.00	0.08	0.00	0.01	0.00	0.01	0.01	0.52	0.11	0.04	0.01
Ti WT%	28.23	27.87	27.93	27.63	28.26	27.57	26.87	28.42	0.44	0.26	0.69	0.43
Zn WT%	0.02	0.00	0.00	0.00	0.00	0.00	0.00	0.00	0.00	0.00	0.00	0.00
Al WT%	0.04	0.01	0.25	0.03	0.04	0.02	0.03	0.03	6.98	0.34	0.20	0.14
Cr WT%	0.04	0.04	0.04	0.04	0.04	0.06	0.04	0.04	0.23	0.17	0.39	0.41
Fe WT%	38.00	38.43	38.04	38.87	38.39	39.15	39.68	37.96	56.46	68.58	68.34	68.42
Mn WT%	0.05	0.03	0.03	0.04	0.06	0.02	0.03	0.02	0.05	0.00	0.00	0.00
Mg WT%	0.34	0.35	0.40	0.37	0.41	0.29	0.27	0.29	0.12	0.04	0.02	0.02
Ca WT%	0.01	0.00	0.01	0.01	0.02	0.02	0.01	0.01	0.17	0.03	0.01	0.01
Na WT%	0.00	0.00	0.01	0.00	0.00	0.00	0.00	0.00	0.11	0.02	0.00	0.00
K WT%	0.00	0.00	0.00	0.01	0.01	0.00	0.00	0.00	0.03	0.01	0.00	0.00
TOTAL	**97.66**	**97.56**	**97.87**	**97.87**	**98.38**	**97.88**	**97.42**	**97.80**	**89.21**	**90.33**	**90.78**	**90.31**
SiO2	0.05	0.00	0.17	0.01	0.01	0.00	0.03	0.02	1.11	0.23	0.09	0.01
TiO2	47.09	46.48	46.59	46.09	47.14	45.98	44.82	47.41	0.73	0.44	1.15	0.71
ZnO	0.03	0.00	0.00	0.00	0.00	0.00	0.00	0.00	0.00	0.00	0.00	0.00
Al2O3	0.07	0.02	0.47	0.06	0.07	0.04	0.06	0.06	13.20	0.63	0.38	0.26
Cr2O3	0.06	0.06	0.05	0.06	0.06	0.09	0.06	0.06	0.33	0.25	0.58	0.60
FeO	48.89	49.44	48.94	50.01	49.39	50.36	51.05	48.84	72.64	88.23	87.92	88.03
MnO	0.06	0.04	0.04	0.06	0.08	0.03	0.04	0.03	0.07	0.00	0.00	0.00
MgO	0.57	0.59	0.67	0.62	0.69	0.48	0.45	0.49	0.19	0.06	0.03	0.03
CaO	0.02	0.00	0.02	0.02	0.03	0.03	0.02	0.02	0.24	0.04	0.02	0.01
Na2O	0.01	0.00	0.01	0.00	0.00	0.00	0.00	0.00	0.14	0.03	0.00	0.00
K2O	0.00	0.00	0.00	0.01	0.01	0.00	0.00	0.00	0.03	0.01	0.00	0.00
TOTAL	**97.66**	**97.56**	**97.87**	**97.87**	**98.38**	**97.88**	**97.42**	**97.80**	**89.21**	**90.33**	**90.78**	**90.31**

	Titanomagnetite			Biotite						
Si WT%	0.02	0.03	0.66	17.58	16.64	16.60	16.77	16.72	16.79	17.10	16.99
Ti WT%	17.09	19.54	10.50	1.96	2.02	2.03	2.06	2.00	1.53	1.43	1.65
Zn WT%	0.00	0.00	0.00	0.03	0.00	0.01	0.00	0.01	0.01	0.01	0.02
Al WT%	0.08	0.09	3.94	10.16	9.34	9.24	9.03	9.10	8.54	9.39	9.13
Cr WT%	0.18	0.09	0.35	0.05	0.05	0.04	0.07	0.05	0.03	0.04	0.04
Fe WT%	50.05	47.72	48.40	11.86	12.01	12.11	12.24	12.30	11.45	9.10	9.38
Mn WT%	0.00	0.03	0.05	0.01	0.01	0.00	0.00	0.01	0.00	0.01	0.00
Mg WT%	0.22	0.35	0.21	7.88	7.22	7.11	7.40	7.37	9.02	9.72	9.74
Ca WT%	0.03	0.01	0.15	0.02	0.02	0.02	0.01	0.00	0.01	0.00	0.04
Na WT%	0.00	0.00	0.14	0.01	0.02	0.02	0.01	0.01	0.01	0.03	0.04
K WT%	0.01	0.01	0.05	8.22	8.38	8.31	8.26	8.39	8.41	8.40	8.21
TOTAL	**94.57**	**95.72**	**90.70**	**98.85**	**94.78**	**94.28**	**94.93**	**95.00**	**95.09**	**95.41**	**95.27**
SiO2	0.04	0.06	1.41	37.60	35.60	35.51	35.89	35.77	35.92	36.57	36.34
TiO2	28.50	32.59	17.51	3.26	3.37	3.39	3.43	3.33	2.56	2.38	2.75
ZnO	0.00	0.00	0.00	0.03	0.00	0.01	0.00	0.01	0.01	0.02	0.02
Al2O3	0.14	0.17	7.45	19.21	17.65	17.46	17.06	17.19	16.13	17.75	17.25
Cr2O3	0.26	0.14	0.51	0.08	0.08	0.05	0.11	0.07	0.05	0.06	0.05
FeO	64.39	61.39	62.27	15.25	15.44	15.58	15.75	15.82	14.73	11.70	12.06
MnO	0.00	0.04	0.07	0.01	0.01	0.00	0.00	0.01	0.00	0.01	0.00
MgO	0.36	0.59	0.34	13.07	11.97	11.80	12.28	12.22	14.96	16.12	16.15
CaO	0.04	0.02	0.21	0.03	0.03	0.03	0.01	0.00	0.01	0.00	0.05
Na2O	0.00	0.00	0.19	0.01	0.03	0.02	0.01	0.01	0.02	0.03	0.05
K2O	0.01	0.01	0.06	9.90	10.09	10.01	9.95	10.10	10.13	10.12	9.89
TOTAL	**94.57**	**95.72**	**90.70**	**98.85**	**94.78**	**94.28**	**94.93**	**95.00**	**95.09**	**95.41**	**95.27**

	Biotite					Cordierite					
Si WT%	17.18	16.26	17.09	17.07	17.10	22.63	22.39	20.52	22.59	22.67	22.64
Ti WT%	1.45	0.72	1.24	1.38	1.42	0.00	0.00	0.01	0.00	0.01	0.00
Zn WT%	0.01	0.00	0.00	0.00	0.00	0.00	0.05	0.00	0.01	0.00	0.04
Al WT%	9.41	10.55	9.55	9.41	9.08	17.52	18.33	20.87	17.70	17.67	17.69
Cr WT%	0.02	0.00	0.01	0.02	0.02	0.00	0.00	0.01	0.00	0.00	0.00
Fe WT%	8.27	9.79	9.14	9.38	9.61	4.74	4.64	7.57	4.68	4.91	4.78
Mn WT%	0.01	0.01	0.01	0.00	0.02	0.00	0.00	0.00	0.01	0.00	0.01
Mg WT%	10.19	9.37	9.68	9.53	9.87	6.09	5.74	3.74	6.15	6.09	6.06
Ca WT%	0.01	0.02	0.02	0.04	0.01	0.00	0.01	0.00	0.00	0.01	0.01
Na WT%	0.03	0.03	0.02	0.04	0.04	0.02	0.02	0.00	0.01	0.01	0.02
K WT%	8.49	8.43	8.16	8.09	8.35	0.00	0.00	0.01	0.00	0.00	0.01
TOTAL	**95.38**	**94.65**	**94.89**	**94.92**	**95.60**	**97.76**	**98.14**	**99.30**	**98.05**	**98.35**	**98.20**
SiO2	36.76	34.79	36.56	36.51	36.59	48.41	47.90	43.89	48.32	48.49	48.44
TiO2	2.42	1.21	2.07	2.30	2.36	0.00	0.00	0.02	0.00	0.01	0.00
ZnO	0.01	0.00	0.00	0.01	0.00	0.00	0.06	0.00	0.01	0.00	0.05
Al2O3	17.78	19.94	18.04	17.78	17.16	33.10	34.64	39.43	33.44	33.39	33.43
Cr2O3	0.03	0.00	0.01	0.04	0.03	0.00	0.00	0.01	0.00	0.00	0.00
FeO	10.64	12.60	11.76	12.07	12.37	6.10	5.97	9.73	6.03	6.31	6.15
MnO	0.01	0.01	0.01	0.00	0.02	0.00	0.00	0.00	0.01	0.00	0.02
MgO	16.90	15.54	16.06	15.81	16.36	10.11	9.52	6.19	10.21	10.10	10.04
CaO	0.02	0.02	0.03	0.06	0.02	0.00	0.01	0.00	0.00	0.01	0.01
Na2O	0.04	0.04	0.03	0.06	0.06	0.03	0.02	0.00	0.01	0.01	0.02
K2O	10.23	10.15	9.84	9.74	10.06	0.00	0.00	0.01	0.01	0.00	0.02
TOTAL	**95.38**	**94.65**	**94.89**	**94.92**	**95.60**	**97.76**	**98.14**	**99.30**	**98.05**	**98.35**	**98.20**

	K-feldspar						
Si WT%	29.63	29.59	29.88	29.62	29.60	29.55	29.79
Ti WT%	0.01	0.00	0.01	0.01	0.01	0.01	0.01
Zn WT%	0.00	0.03	0.00	0.00	0.02	0.01	0.01
Al WT%	9.71	9.76	9.73	9.67	9.84	9.74	9.70
Cr WT%	0.01	0.01	0.00	0.00	0.01	0.01	0.01
Fe WT%	0.01	0.03	0.00	0.11	0.13	0.02	0.06
Mn WT%	0.00	0.00	0.01	0.01	0.00	0.00	0.00
Mg WT%	0.00	0.00	0.00	0.03	0.09	0.00	0.00
Ca WT%	0.01	0.02	0.01	0.03	0.02	0.01	0.01
Na WT%	0.18	0.16	0.14	0.19	0.15	0.11	0.12
K WT%	13.78	13.75	13.90	13.66	13.61	14.07	13.98
TOTAL	**98.93**	**99.03**	**99.67**	**99.00**	**99.30**	**99.26**	**99.53**
SiO2	63.38	63.30	63.92	63.37	63.32	63.23	63.74
TiO2	0.01	0.00	0.01	0.01	0.01	0.02	0.01
ZnO	0.00	0.03	0.00	0.00	0.03	0.02	0.01
Al2O3	18.35	18.44	18.38	18.26	18.60	18.40	18.33
Cr2O3	0.02	0.01	0.00	0.00	0.02	0.01	0.02
FeO	0.01	0.04	0.00	0.14	0.16	0.03	0.08
MnO	0.00	0.00	0.01	0.01	0.00	0.00	0.00
MgO	0.00	0.00	0.00	0.04	0.14	0.00	0.00
CaO	0.02	0.03	0.01	0.04	0.03	0.01	0.01
Na2O	0.24	0.21	0.18	0.25	0.20	0.15	0.16
K2O	16.60	16.56	16.75	16.46	16.39	16.95	16.84
TOTAL	**98.93**	**99.03**	**99.67**	**99.00**	**99.30**	**99.26**	**99.53**

APPENDIX 4: MELT LOSS COMPOSITIONS

Measured compositions of the greenschists and granulites, with the calculated melt loss compositions, all in mol%.

	Greenschist	6% Melt Loss	12% Melt Loss	18% Melt Loss	Granulite
H_2O	6.09	4.94	3.75	2.95	2.66
SiO_2	73.30	73.94	74.56	74.85	72.96
Al_2O_3	8.95	9.09	9.25	9.38	10.89
CaO	0.07	0.03	0.01	0.01	0.07
MgO	2.81	2.99	3.17	3.36	5.35
FeO	5.09	5.40	5.74	6.06	4.35
K_2O	3.06	2.98	2.87	2.71	2.60
Na_2O	0.09	0.06	0.03	0.02	0.08
TiO_2	0.38	0.41	0.43	0.46	0.57
MnO	0.03	0.03	0.04	0.04	0.04
O	0.13	0.14	0.15	0.16	0.44

APPENDIX 5: CATASTROPHIC MELT LOSS

Catastrophic melt loss calculations from the greenschist bulk composition (Figure **), in mol%. The real greenschist and granulite compositions are shown, with the compositions that were calculated from extracting the percentage of melt shown in each column in a single melt loss event form the greenschist composition.

	Greenschist	18% Catastrophic Melt Loss	20% Catastrophic Melt Loss	25% Catastrophic Melt Loss	30% Catastrophic Melt Loss	35% Catastrophic Melt Loss	40% Catastrophic Melt Loss	45% Catastrophic Melt Loss	50% Catastrophic Melt Loss	55% Catastrophic Melt Loss	Granulite
H_2O	6.09	3.410	3.294	2.983	2.477	1.658	1.624	1.624	1.598	1.498	2.66
SiO_2	73.30	74.434	74.395	74.357	74.345	74.494	74.062	73.548	72.955	72.371	72.96
Al_2O_3	8.95	9.340	9.373	9.451	9.567	9.734	9.787	9.84	9.936	10.257	10.89
CaO	0.07	0.011	0.016	0.024	0.031	0.04	0.037	0.03	0.024	0.018	0.07
MgO	2.81	3.393	3.465	3.623	3.850	4.117	4.407	4.741	5.128	5.455	5.35
FeO	5.09	6.104	6.22	6.479	6.854	7.031	7.751	8.261	8.852	9.106	4.35
K_2O	3.06	2.620	2.532	2.348	2.088	1.804	1.422	0.975	0.441	0.119	2.60
Na_2O	0.09	0.024	0.022	0.018	0.021	0.029	0.023	0.016	0.008	0	0.08
TiO_2	0.38	0.467	0.479	0.503	0.538	0.578	0.624	0.678	0.742	0.823	0.57
MnO	0.03	0.039	0.04	0.042	0.045	0.048	0.052	0.056	0.062	0.068	0.04
O	0.13	0.159	0.163	0.172	0.184	0.197	0.213	0.232	0.254	0.281	0.44

APPENDIX 6: MELT FERTILITY

Melt produced in an open system where melt is drained periodically VS a closed system where all melt remains within the system throughout the duration of melting.

Temperature (°C)	Melt produced in open system (%)	Melt produced in closed system (%)
700	0.8	0.8
710	9.0	10.8
720	15.0	14.8
730	15.2	15.4
740	15.3	16.1
750	15.5	16.9
760	15.7	17.7
770	15.9	18.8
780	16.5	20.3
790	17.7	22.4
800	19.6	25.0

APPENDIX 7: MELT REINTEGRATION COMPOSITIONS

Measured compositions of the greenschists and granulites, with the calculated melt reintegration compositions all in mol%.

	Granulite	6% Melt Reintegration	12% Melt Reintegration	18% Melt Reintegration	Greenschist
H_2O	2.66	3.40	5.08	6.18	6.09
SiO_2	72.96	72.76	71.85	71.25	73.30
Al_2O_3	10.89	10.72	10.45	10.26	8.95
CaO	0.07	0.11	0.14	0.15	0.07
MgO	5.35	5.06	4.78	4.51	2.81
FeO	4.35	4.13	3.90	3.68	5.09
K_2O	2.60	2.74	2.78	2.81	3.06
Na_2O	0.08	0.102	0.173	0.296	0.09
TiO_2	0.57	0.53	0.50	0.48	0.38
MnO	0.04	0.04	0.04	0.03	0.03
O	0.44	0.412	0.389	0.367	0.13